9-7-2021

RAINBOW TRAPPING EFFECT IN 2D AXISYMMETRIC BROADBAND ACOUSTIC ENERGY HARVESTERS

Louis Alexander Gormley
Rowan University

RAINBOW TRAPPING EFFECT IN 2D AXISYMMETRIC BROADBAND ACOUSTIC ENERGY HARVESTERS

by
Louis A. Gormley

A Thesis

Submitted to the
Department of Mechanical Engineering
College of Engineering
In partial fulfillment of the requirement
For the degree of
Master of Science in Mechanical Engineering
at
Rowan University
August 27, 2021

Thesis Chair: Chen Shen, Ph.D.

Committee Members:
Behrad Koohbor, Ph.D.
Hong Zhang, Ph.D.

Acknowledgements

I would like to extend my sincerest gratitude to Dr. Chen Shen for his guidance and patience throughout the research process for this project. Furthermore, I wish to express my appreciation to Charles ”Chuck” Linderman and Karl Dyer for their assistance with manufacturing the physical acoustic energy harvester prototypes. The contributions of Dr. Shen, Chuck Linderman, and Karl Dyer proved invaluable while completing this study. Additionally, I would like to thank Dr. Behrad Koohbor and Dr. Hong Zhang for their service on my thesis defense committee.

Moreover, I wish to thank Masoome Maroufi for her continued support and inspiration.

Abstract

Louis A. Gormley
RAINBOW TRAPPING EFFECT IN
2D AXISYMMETRIC BROADBAND ACOUSTIC ENERGY HARVESTERS
2020-2021
Chen Shen, Ph.D.
Master of Science in Mechanical Engineering

Acoustic energy harvesters (AEHs) collect otherwise unused ambient acoustic waves for conversion into useful electrical energy. This promising technology has potential applications ranging from grid-independent electronics to structural health monitoring systems. AEHs capture specific acoustic frequencies of interest using structures with frequency-matched component geometries. Despite the multitude of potential geometries suitable for AEH structures, existing AEH research has predominantly focused on the acoustic wave trapping performance of unidimensional or linear bidimensional AEH structures.

This study intended to broaden AEH bandwidth and capture efficiency by investigating the acoustic rainbow trapping performance of a novel 2D axisymmetric AEH design. A Finite Element Method (FEM) approach was employed using COMSOL Multiphysics® v5.5 to evaluate the acoustic wave trapping performance of various groove, cylindrical pillar, and circular hole-based unit cell geometries across the 100 kHz - 220 kHz frequency range. The grooved unit cell groove/plate depth ratio and overall plate depth were optimized. A FEM simulation analyzed the acoustic rainbow trapping performance of a 2D axisymmetric AEH design comprised of a gradient array of these optimized unit cells. These FEM results were validated using an array of piezoMEMS sensors mounted to an aluminum AEH prototype.

The prototype displayed reliably predictable acoustic frequency trapping at defined locations. Through these results, this study demonstrated the viability of 2D axisymmetric AEHs in enhancing the acoustic rainbow trapping effect across a broadband frequency range of interest. However, there is much opportunity to refine this AEH design. This proof of concept presents a strong impetus for furthering 2D axisymmetric AEH research.

Table of Contents

Table of Contents (Continued)

Table of Contents (Continued)

Table of Contents (Continued)

List of Figures

Figure Page

List of Figures (Continued)

Figure Page

List of Tables

Table Page

Chapter 1

Introduction

1.1 Energy Harvesting

Throughout history, humanity has attempted to harness every available form of energy to achieve useful goals. From transforming chemical energy into thermal energy via combustion in prehistoric times to converting sunlight into electrical energy with photovoltaic panels in the modern era, energy conversion and transmission have played a crucial role in the development of human civilization. Humanity's ongoing quest to master energy conversion and transmission has provided a multitude of benefits to all of its activities.

Until relatively recently, acoustic vibrations have been largely overlooked as a viable energy source. Instead, they have traditionally been viewed primarily as a nuisance or source of wasted energy without significant opportunity for recovery [1]. However, acoustic energy harvesters (AEHs) intend to change that situation by extracting useful work from an otherwise untapped energy source.

1.2 Acoustic Energy Harvesters — piezoMEMS Collectors

Acoustic energy harvesters are part of a relatively new field that aims to transform kinetic energy from acoustic waves (phonons) into electrical current, most commonly in conjunction with piezoelectric microelectromechanical systems (MEMS) transducers. Piezoelectric MEMS, or piezoMEMS as they are also known, rely on the piezoelectric effect where piezoelectric materials collect electric charges when they are subjected to mechanical stress. When connected in a circuit with other electrical devices such as batteries or supercapacitors, electrical charges collected by piezoMEMS devices can be transferred to another device for storage and later use [2].

Common piezoelectric materials include:

1. Crystalline materials such as
    (a) Quartz and
    (b) Topaz;
2. Ceramic materials such as
    (a) Lead zirconate titanate (PZT) and
    (b) Zinc oxide (ZnO); and
3. Polymers such as
    (a) Polyvinylidene fluoride (PVDF) and
    (b) Polyvinylidene chloride (PVDC).

Lead zirconate titanate (PZT) is one of the most frequently used piezoelectric materials for piezoMEMS applications due to its inexpensive production cost, suitability for customization, high relative permittivity, and overall physical strength. PiezoMEMS collectors made of PZT are typically packaged as integrated devices using rigid metallic discs. While piezoMEMS collectors can harvest energy from vibrations in a standalone configuration, the collectors' performance is constrained by their physical contact with the vibrations of interest. When coupled with acoustic energy harvesting structures, piezoMEMS collectors can reach their peak potential vibration energy harvesting capabilities.

1.3 Acoustic Energy Harvesters — Structures

Acoustic energy harvesters consist of structures capable of trapping acoustic waves of frequencies of interest. Such energy harvesters intend to enhance predictable frequency trapping at known physical locations to maximize vibration contact with piezoMEMS collectors, electromagnetic collectors, or other devices.

These structures are often made using acoustic metamaterials. Acoustic metamaterials and phononic crystals intend to control and manipulate acoustic waves using engineered structures to improve wave-matter interactions [3]. While phononic crystals act within the wavelength scale, acoustic metamaterials are effective on the sub-wavelength scale. Such metamaterials rely on periodically varying their acoustic materials properties such as mass and elasticity to change the phase velocity of waves traveling through them. When used in acoustic energy harvesters, acoustic metamaterials work to result in one or more band gaps. They are designed to trap certain frequencies of interest at predictable physical positions within the acoustic energy harvester structure. Acoustic metamaterials achieve this selective frequency trapping primarily by changing the density (ρ) and bulk modulus (β) of the acoustic carrier medium. These changes cause a variation in the acoustic refractive index, and this directly influences the behavior of acoustic waves traveling through the acoustic metamaterial.

Many acoustic energy harvesters can be further improved through wave manipulation taking advantage of the rainbow trapping effect. Rainbow trapping has the potential to widen the bandwidth of a given acoustic energy harvester, thereby increasing energy harvesting efficiency and the overall quantity of harvested energy.

1.4 Rainbow Trapping Effect

The rainbow trapping effect concerns a gradient change in the group velocity of waves traveling through a given structure. This gradual change in group velocity causes subfrequencies within a wave to settle at different locations within an energy harvester structure. The rainbow trapping effect was initially proposed for use in optical energy harvesting applications in 2007 [4]. However, rainbow trapping effect research quickly spread to acoustic applications. The first acoustic energy harvester demonstrating the rainbow trapping effect using a grooved structure was unveiled in 2013 [5].

Any given acoustic input wave can carry a multitude of subfrequencies, and the

rainbow trapping effect illustrates how subfrequencies of interest can be separated from an input wave. An acoustic energy harvester's structure can be finely tuned to trap specific subfrequencies at precise physical locations within the energy harvester's structure. Energy harvesting performance therefore improves as the appropriate energy harvesting devices such as piezoMEMS collectors can be placed within the energy harvester's relevant areas of interest.

While acoustic energy harvesting using the rainbow trapping effect is a relatively new field, a growing number of works have been published regarding the rainbow trapping effect, acoustic energy harvester structures, acoustic metamaterials, and applications of acoustic energy harvesters.

Chapter 2

Literature Review

2.1 Acoustic Energy Harvesting Overview

Acoustic energy harvesters intend to achieve peak energy conversion efficiency through maximizing various acoustic wave trapping effects such as the rainbow trapping effect. Understanding acoustic wave behavior is critical for designing an optimal AEH. Acoustic wave propagation in fluids can be modeled through three primary equations [3]:

$$\rho \frac{\partial \mathbf{v}}{\partial t} = -\nabla p \tag{1}$$

$$\frac{\partial p}{\partial t} + K\nabla \cdot \mathbf{v} = 0 \tag{2}$$

$$\frac{\partial^2 p}{\partial^2 t} = \frac{K}{\rho}\nabla^2 p \tag{3}$$

Equation 1 illustrates the relationship between acoustic pressure p, acoustic particle perturbation velocity $\mathbf{v}$, and fluid mass density ρ. This relationship is derived from Newton's first law of motion ($F = ma$), and it highlights the importance that both fluid mass density and acoustic particle perturbation velocity have in the resulting acoustic pressure. Similar to the force component of Newton's first law, acoustic pressure is the primary driver behind an acoustic wave's propagation throughout a given medium.

The relationship between the compression and expansion of a stationary nonviscous fluid and the movement of said fluid also plays an important role in acoustic wave behavior. Assuming that acoustic wave propagation is an isentropic process so that any thermal components may be ignored, combining the conservation of mass with this assumption results in Equation 2. This equation illustrates the significance of the fluid's resistance to

compression, bulk modulus K, with respect to the acoustic particle perturbation velocity.

While both of these equations are useful for studying acoustic wave behavior in fluids, combining both equations to solve for acoustic pressure using the fluid bulk modulus and mass density results in the greatest insight into a wave's propagation characteristics. This combined equation, Equation 3, defines the acoustic wave velocity c as the relationship between a fluid's bulk modulus and its mass density.

$$c = \sqrt{\frac{K}{\rho}} \tag{4}$$

The acoustic wave velocity influences a wave's directional change as it encounters interfaces between media. Equation 5 defines the acoustic wave impedance Z, a direct influence on the amplitude of a wave's transmission and reflection between media interfaces.

$$Z = \sqrt{K\rho} = \frac{p}{v} \tag{5}$$

With these equations, it is clear that the primary determinants of acoustic wave propagation throughout a given fluid are fluid mass density ρ and bulk modulus K. As such, these are the underlying physical parameters that the AEH design optimization process seeks to influence. While the aforementioned equations explain the propagation of acoustic waves through a fluid, they do not directly explain how a structure may be used to extract useful energy from low levels of natural environmental acoustic pressure.

Helmholtz resonators amplify incident acoustic waves for enhancing overall energy capture. A Helmholtz resonator is a simple mass-spring-damper system using a physical cavity and neck geometry with rigid walls [6]. This may be modeled as mechanical system with a single degree of freedom where it is possible to calculate the structural acoustic resonant frequency. Equation 6 defines a given structure's acoustic resonant frequency f.

$$f = \frac{c}{2\pi}\sqrt{\frac{s}{V(l+\gamma a)}} \tag{6}$$

This equation focuses on the speed of sound through the medium of interest c, neck cross-sectional area s, neck length l, cavity volume V, correction factor γ, and open neck radius a. An acoustic pressure difference exists between the interior of the resonator and the external environment. This pressure difference drives the resonator structure to capture more acoustic energy from its environment than would otherwise be captured.

While Helmholtz resonators boost localized acoustic pressure over ambient acoustic pressure levels, they are somewhat limited in their application. Planar acoustic metamaterials offer an effective energy harvesting alternative to Helmholtz resonators by designing specific defects within an otherwise perfect acoustic metamaterial to trap desired acoustic waves [7]. Both structures amplify localized acoustic pressure over ambient acoustic pressure levels, but planar acoustic metamaterials offer decreased structural complexity. Such acoustic metamaterials may be tuned for a wider variety of acoustic frequencies compared to discrete Helmholtz resonators since individual metamaterial defects may use a higher density configuration. Perfect acoustic absorption is rare when transmission is permitted, so asymmetric microstructures may enhance a structure's overall acoustic absorption [8].

Solid structures present more complex acoustic wave behavior compared to fluids. Acoustic waves in solids consist of opposing inertial and elastic forces seeking equilibrium. Wave velocity in solids increases with Poisson's ratio ν and Young's modulus E but decreases with density ρ [9]. Unit cells may be tuned with periodic variations in these parameters to control the wave's group velocity and either stop or permit transmission of elastic waves. However, the medium and wave properties both heavily influence the result.

The range of frequencies for which a solid structure prevents wave propagation is known as its band gap. While a discrete solid structure may have multiple propagating modes, acoustic energy within a band gap is concentrated at discrete locations since it cannot flow through the structure [9]. Subsequently, larger band gaps provide greater acoustic wave capture opportunity. AEH structures are specifically designed to maximize their band gap and convert the acoustic waves trapped within it into electrical energy.

2.2 Energy Conversion Devices

While a multitude of energy conversion devices such as motors and thermoelectric generators may work with various energy sources, acoustic energy harvesters are much more limited with regards to their appropriate pairing of energy conversion devices. The ultimate goal of an acoustic energy harvester is to convert acoustic energy into another type of energy, usually in the form of electrical energy. Of energy conversion devices suitable for converting acoustic energy into electrical energy, piezoMEMS devices and electromagnetic converters are the typical selections for acoustic energy harvesters [6].

2.2.1 Piezoelectric MEMS (PiezoMEMS)

Piezoelectric microelectromechanical systems (piezoMEMS) are micrometer-scale devices with typically high surface area to volume ratios. PiezoMEMS devices use piezoelectric materials to convert mechanical stress into useful electrical energy. When a piezoelectric material such as lead zirconate titanate (PZT) is subjected to mechanical stress, electric charge accumulates within the material. The accumulated electric charge can then be transported via a conductor to devices consuming electrical energy. A piezoMEMS device is comprised of piezoelectric material, localized conductor material, and a compatible substrate material in one cohesive package to maximize the collection of electrical energy from induced mechanical stress.

These energy harvesting devices are particularly useful due to their relatively simple construction and small physical packaging. PiezoMEMS are typically made of substrate, piezoelectric material, and conductor layers, and the combined layers result in a thin sensor package [10]. This allows piezoMEMS energy harvesters to be used in applications where device thickness is intended to be minimized while still maintaining a high energy harvesting density capability. Many potential applications exist where piezoMEMS would be the only currently available energy harvesting devices suitable for the the application's needs.

2.2.2 *Electromagnetic Converters*

In contrast to the relatively flat, thin, and simple piezoMEMS devices, electromagnetic energy converters tend to be taller and more massive with greater overall complexity. As their name implies, electromagnetic AEH structures use an electromagnet as their core energy conversion device. Electromagnetic AEHs consist of a wound electric coil, flexible membrane, and permanent magnet housed within a Helmholtz resonator cavity. Air enters through a cavity at the top of the Helmholtz resonator cavity, and it exits the cavity near the permanent magnet installed at the bottom of the cavity [2]. The flexible membrane catches airflow similar to a sail as it travels through the resonator cavity. As the increased acoustic pressure inside the Helmholtz resonator cavity pushes the coil towards the permanent magnet, the induced magnetic field results in an electrical current flow from the coil to an external energy storage device. Figure 1 illustrates both a cross-section and exploded view of a typical electromagnetic AEH assembly.

Figure 1

Electromagnetic Acoustic Energy Harvester Design [2]

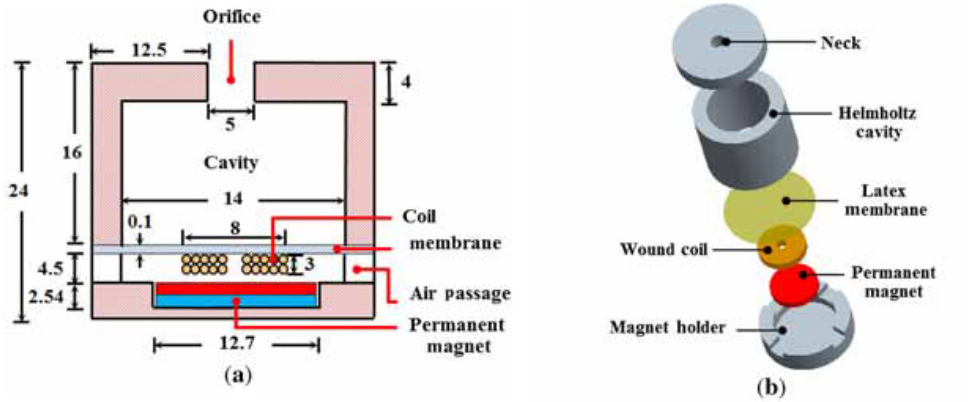

(a) *Electromagnetic AEH cross-section* **(b)** *Electromagnetic AEH components*

2.3 Acoustic Metamaterials — Structural Behavior

2.3.1 Structural Overview

The unit cell is the fundamental base component of AEH structures. Unit cells represent the smallest discrete acoustic structures within a defined geometry. While unit cell geometry is somewhat arbitrary, squares are often used for simplicity in analysis. AEH structures consist of one or more arrays of repeating or varying unit cells working in unison to capture acoustic waves.

Unit cells are primarily separated into bending-dominated and stretch-dominated varieties. As their names imply, bending-dominated unit cells tend to experience perimeter wall bending when subjected to external forces, and stretch-dominated unit cells tend to experience internal structural stretching when subjected to the same external forces. At low frequencies, both unit cell types behave as homogeneous metamaterials since the unit cell side lengths are significantly smaller than the Bloch wavelength for the frequency of interest [11]. This is a useful assumption when designing an effective AEH structure since both unit cell types can be predictably and reliably used in an array for macroscale AEHs.

Labyrinthine metasurface structures are prominent examples of AEH structures combining multiple unit cell designs with uniquely differing properties to achieve enhanced macroscale AEH performance. Aptly named, labyrinthine metasurface structures consist of a coiled channel with winding and potentially interlocking pathways resembling a maze or labyrinth [12]. These winding pathways may have differing geometries, dimensions, or arrangement configurations, and these properties directly influence which frequencies of acoustic waves are trapped at specific locations within the labyrinthine structure. This type of AEH structure may offer a wide range of acoustic frequencies with effective AEH performance due to its high feature density, but manufacturing such structures is somewhat difficult due to the scale and feature complexity of the individual labyrinthine channels. However, simpler alternatives exist that still retain broadband AEH capability.

Rainbow trapping acoustic metamaterials are one such alternative to labyrinthine metasurface structures. Similar to labyrinthine metasurface structures, acoustic metamaterials rely on an ordinary waveguide consisting of an array of discrete unit cell structures to achieve acoustic rainbow trapping across a range of frequencies. The structures used in this ordinary waveguide direct acoustic waves traveling across the AEH structure, and they are typically simpler and easier to manufacture compared to their labyrinthine metasurface counterparts. Figure 2 illustrates an example of a rainbow trapping acoustic metamaterial.

Figure 2

Acoustic Metamaterial Configuration — Rainbow Trapping [5]

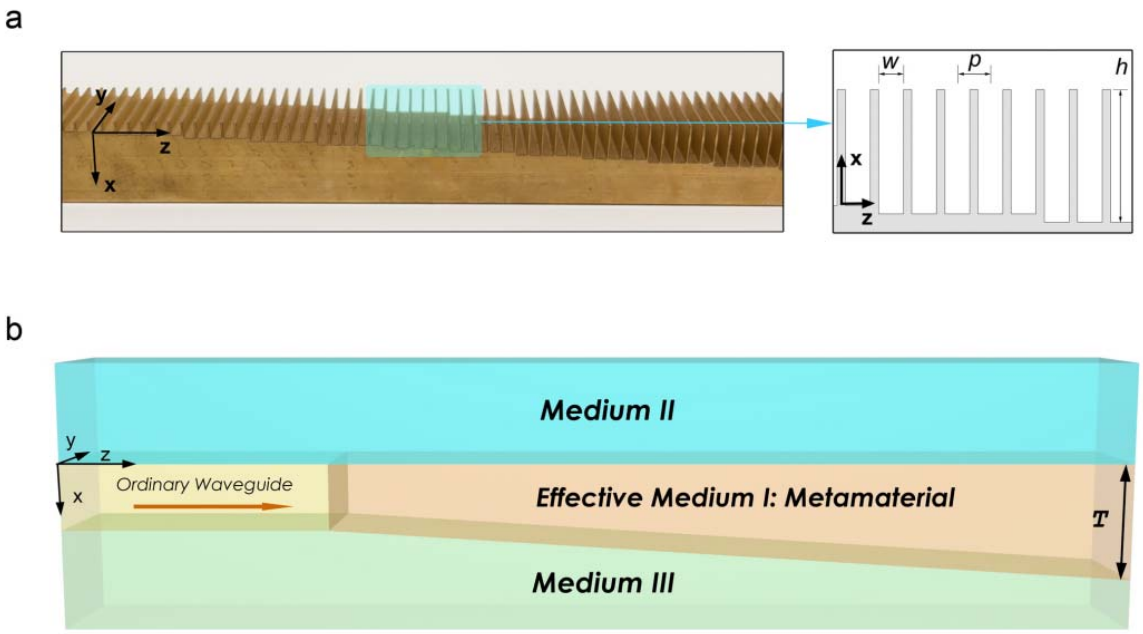

(a) *Example of a rainbow trapping acoustic metamaterial with constant groove width (w) and extrusion width (p) and variable fin height (h)*, **(b)** *Acoustic metamaterial composite structure*

As is illustrated by this figure, an acoustic metamaterial composite structure consists of three effective media:

1. The acoustic metamaterial itself;

2. The primary conveyor of acoustic waves (typically air); and

3. The AEH support substrate (usually the same material as the acoustic metamaterial).

Geometric variations in Medium I's unit cells guide acoustic waves from Medium II to trap frequencies at discrete locations and transmit trapped waves to Medium III. Energy conversion devices in Medium III then convert these waves into electrical energy.

2.3.2 Structure Geometries

Unit cell geometries are critical in determining the frequencies which an AEH will effectively capture acoustic waves. Typical AEH structure geometries include [13]:

1. Grooves;

2. Cylindrical or prismatic pillars; and

3. Cylindrical or squared holes.

Figure 3 illustrates examples of these three typical AEH unit cell geometries.

Figure 3

Typical Acoustic Energy Harvester Geometries

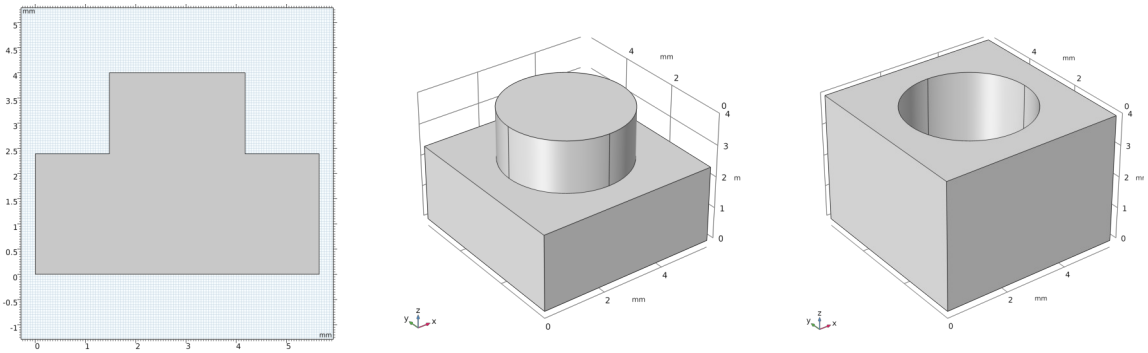

(a) *Grooves* **(b)** *Pillars* **(c)** *Holes*

As can be seen in this figure, grooves are the simplest overall geometry consisting of a solid structure with grooves cut into the upper sides of the unit cell. This simple geometry corresponds to a greater ease of manufacturing since grooves can be easily produced with common manufacturing techniques such as milling, filing, or even laser cutting. Pillars are somewhat more complex since they can be of varying shape. Both prismatic and cylindrical pillars have been used in existing AEH applications, but these are more difficult to manufacture compared to simple grooves. The circular component of cylindrical pillars adds additional complexity to the manufacturing process since any given cutting motion must include movement on two axes. Prismatic or hexagonal holes and pillars share similar manufacturing challenges. Conversely, cylindrical holes are easier to manufacture since they can be produced with a single circular drill. Other groove, pillar, and hole geometries are also possible, but these are the most common and easily reproducible examples.

2.4 Preexisting Work

2.4.1 Grooved Acoustic Energy Harvesters

Grooved AEH structures are similar in appearance to acoustic metamaterials, and they mostly share comparable functionality. These structures rely on an array of transversely-aligned unit cells of varying acoustic properties to capture the acoustic frequencies of interest. While grooved AEH structures may appear unsophisticated compared to more complicated designs such as labyrinthine metasurface structures, grooved structures offer reasonable AEH performance with simpler manufacturing requirements.

A grooved AEH unit cell n is defined by its plate height h, groove depth d, extrusion width s, and unit cell width Δ_n. Its substrate thickness t is merely the difference between the plate height h and the groove depth d. While grooves can be rectangular, chevron-shaped, rounded, or another shape, rectangular grooves are typically the simplest to design and manufacture. This results in a cost advantage for AEHs using rectangular grooves. Figure 4 illustrates a type of grooved AEH called a chirped phononic crystal plate.

Figure 4

Grooved AEH Structure [14]

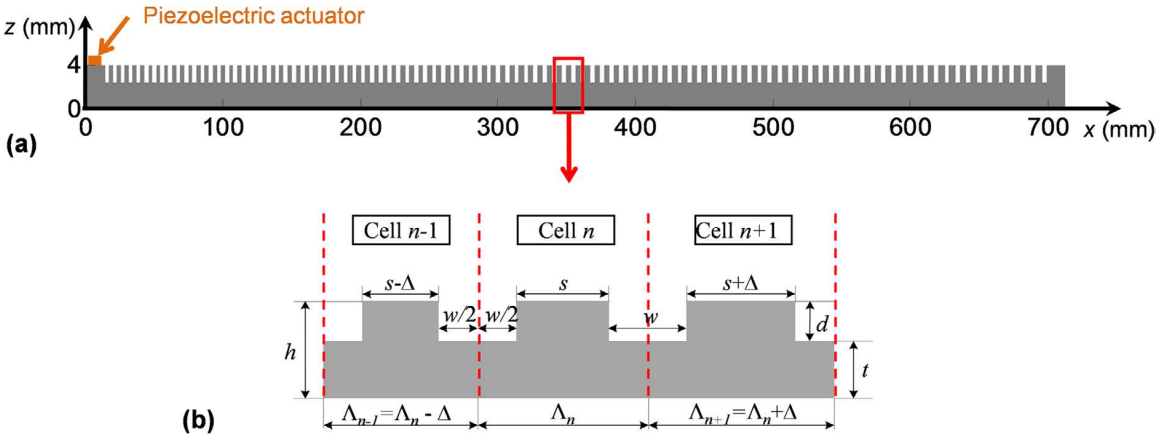

(a) *Chirped phononic crystal plate cross-section*,

(b) *Unit cells of width* (Λ_n) *defined by constant groove width* (w) *and variable extrusion width* (s_n)

Phononic crystals rely on periodic variations to alter their acoustic properties at different locations within the structure. The acoustic variations result in a situation where certain acoustic frequencies are trapped at a given location within the structure, and these frequencies are not permitted to transmit throughout the rest of the structure. This trapping effect serves as the functional basis behind AEHs since the trapped waves can be converted into usable electrical energy using a suitable energy conversion device. The structure's prohibition on transmission for certain frequencies at different locations creates a band gap across the structure, and this band gap represents an AEH's wave trapping potential.

Due to their relative geometric simplicity, grooved AEH structures offer a limited number of physical parameters to influence their acoustic wave capture performance. Of the available parameters, groove width and extrusion width are two of the most common parameters to vary for specific acoustic frequency trapping. This is largely due to the mechanism of interaction between acoustic waves and the AEH structure. Waves tend to travel along the length of an AEH structure that is placed on an unrelated surface due to the differences in boundary conditions between the surfaces of the AEH. As a result,

waves primarily interact with the AEH structure in the same direction as the AEH's unit cell width. This means that the unit cell's width parameters have the greatest influence on acoustic wave trapping. With this in mind, width-graded grooved AEH structures can provide excellent and continuously repeatable acoustic rainbow trapping performance [15].

Gradient AEH structures build upon the aforementioned principles by continuously varying one primary AEH unit cell parameter across the span of the AEH structure. This gradient variation in the unit cells provides for a gradual slowing of acoustic waves as they travel across the AEH structure. Similar to phononic crystals, gradient AEH structures provide predictable wave trapping locations for specified acoustic frequencies. This allows gradient AEH structures to achieve high acoustic energy conversion potential. One prominent example of a gradient acoustic metamaterial involves a rectangular grooved structure with progressively increasing groove depth along the length of the AEH structure [16]. This design offers the same ease of design and manufacturing benefits as other grooved AEH structures while enhancing the acoustic rainbow trapping effect when certain boundary conditions apply to the AEH. While this example demonstrates a gradient AEH structure's performance capabilities, these abilities are not solely restricted to grooved types of AEH structures. Other geometries such as pillars or holes may also be used as the acoustic elements in gradient AEH structural design.

2.4.2 Pillar-Based Acoustic Energy Harvesters

In contrast to grooved AEHs, pillar-based AEHs consist of an array of discrete pillar elements. These pillars may be made of cylinders [17], triangular [18], rectangular [19], or hexagonal prisms, or any other type of extruded shape. Pillar-based AEH designs also benefit from their potential to dramatically reduce the acoustic wave propagation speed and to selectively capture specific frequencies of interest through an acoustic rainbow trapping effect. Such AEH structures may employ uniform [20] or gradient [19] unit cells. Figure 5 illustrates an example of an AEH using an array of uniform cylindrical pillar unit cells.

Figure 5

Cylindrical Pillar-Based AEH Structure

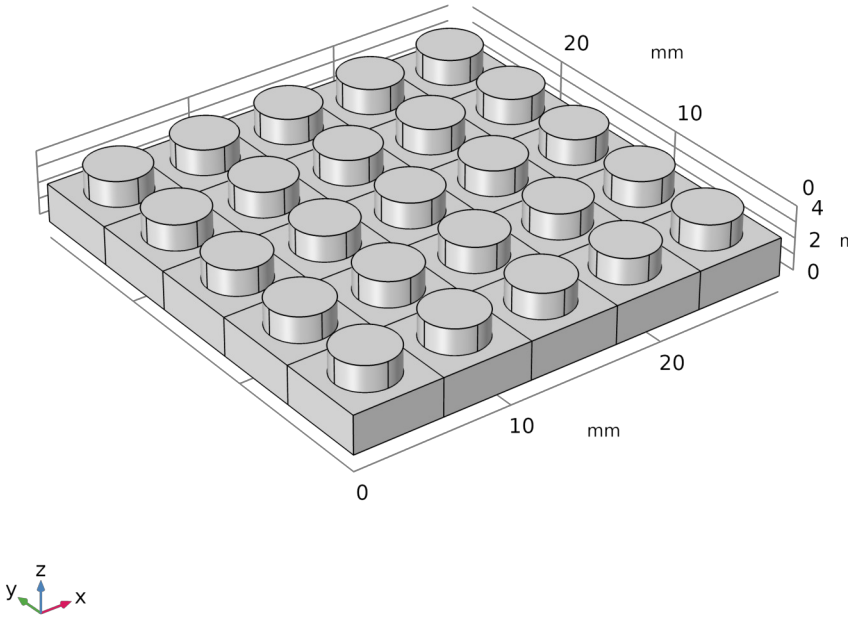

Both uniform and gradient pillar-based AEH structures can be quite effective at broadband acoustic wave trapping, but uniform unit cells result in a simpler design at the expense of the acoustic rainbow trapping performance offered by gradient unit cells. Pillar-based AEHs are typically more difficult to manufacture from a single piece of material than grooved-based AEHs using traditional subtractive manufacturing processes since extrusion-type features require additional material cuts in multiple directions. Conversely, pillar-based AEHs may be simpler to construct on a large scale from individual components since the components may be assembled using common hand tools. Figure 6 illustrates an example of a large-scale, gradient, prismatic pillar-based AEH structure.

Figure 6

Prismatic Pillar-Based AEH Structure [19]

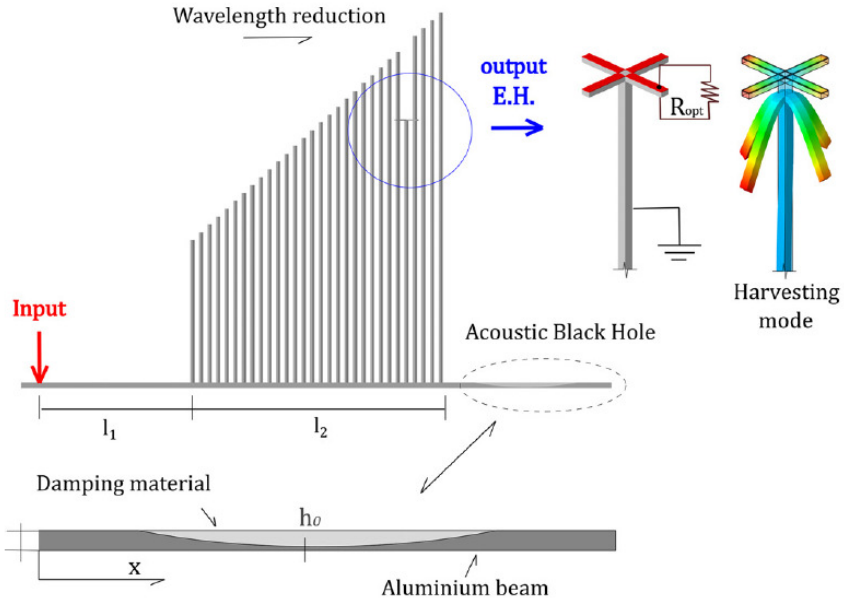

This AEH example particularly benefits from enhanced material stress experienced at the upper surface of the pillar elements since this acoustic wave-induced stress is converted to electrical energy using piezoMEMS devices mounted at that location. However, this differs from typical gradient pillar-based AEH designs with high acoustic rainbow trapping performance where the piezoMEMS devices are mounted to the bottom AEH substrate [21]. In this case, an interior pillar element is intentionally shortened compared to the overall pillar height gradient present across the structure to evaluate the AEH structure's rainbow trapping performance at that interior location with reduced pillar height.

Furthermore, these pillar elements can be tuned for capturing specific frequencies of interest simply by adding or removing mass from the top of the pillars [22]. This is a unique advantage of pillar-based AEH structures that offers an increased amount of flexibility regarding the AEH's design for effectively trapping a given range of acoustic frequencies. In summary, pillar-based AEH structures offer a good balance between the adaptability of their acoustic wave trapping performance and any ease of manufacturing trade-offs.

2.4.3 Hole-Based Acoustic Energy Harvesters

Holes are essentially inverted pillars where material is subtracted from instead of added to the substrate. Likewise, hole-based and pillar-based AEHs may share similar unit cell feature geometries. These feature geometries include circular [23], triangular, rectangular [24], hexagonal [25], or other hole shapes. However, circular holes have a clear manufacturing advantage since they may be made with one simple drilling motion. Blind holes extend partway through and through-holes extend entirely through the AEH structure. Figure 7 illustrates an AEH comprised of an array of uniform, circular, blind hole unit cells.

Figure 7

Hole-Based AEH Structure

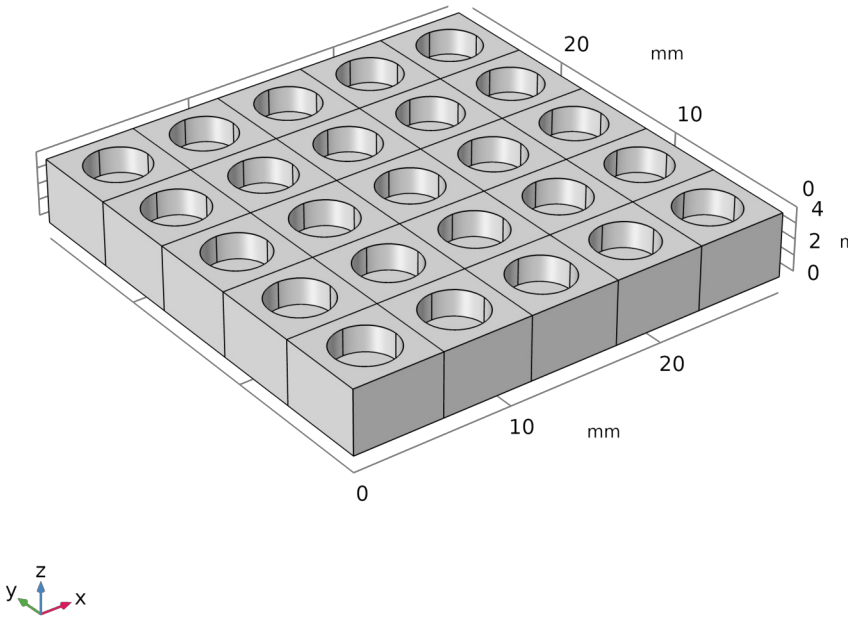

Alternative unit cell feature geometries would require more complex manufacturing processes involving additional movements or tools, and this would lead to a corresponding production cost premium over circular holes. On the other hand, more complex hole geometries may be economically produced using certain casting or stamping techniques if the substrate material is suited to these manufacturing processes. Regardless, hole-based AEH structures generally exhibit a similar level of design and manufacturing difficulty as their groove-based counterparts.

Arrays of hole-based unit cells generally form metasurface structures where acoustic waves travel across the surface and are trapped with the hole structures [24]. The diameters, depths, and positioning density of these hole-based unit cells directly influences which acoustic frequencies are trapped by the AEH structure. Rainbow trapping hole-based AEHs use a an array of unit cells that vary these physical properties to trap specific acoustic frequencies of interest [23]. This method generally results in greater broadband AEH performance than uniform periodic metamaterials since it provides wider band gaps across a wider range of acoustic frequencies. This causes a corresponding increase in the overall wave capture potential for an AEH structure with a similar physical footprint.

2.4.4 Coiled Acoustic Energy Harvesters

Similar to labyrinthine metasurfaces, coiled AEH structures capture acoustic waves using winding channels [26]. These winding channel structures also benefit from gradient unit cells since they generally exhibit improved gradual slowing and selective trapping of acoustic waves across the structure. The waveguide is sandwiched between two winding channel unit cell layers, and acoustic waves are trapped by the frequency-matched unit cell. This provides excellent acoustic wave containment within the AEH structure. However, this arrangement involves increased manufacturing difficulty due to the winding nature of the channels and the doubled number of individual unit cells required by the AEH structure. Figure 8 illustrates an example coiled AEH design with gradient unit cells.

Figure 8

Coiled AEH Structures [27]

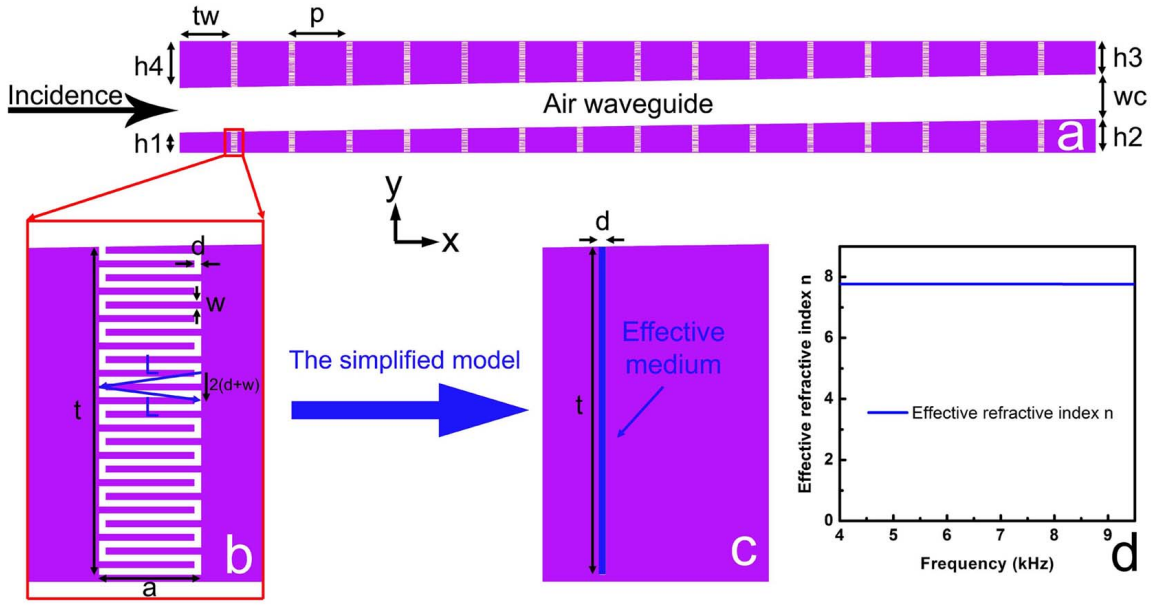

(a) *Air waveguide with variable height space-coiling cells*, **(b)** *Wave propagation detail within a given space-coiling cell*, **(c)** *Condensed comparison of space-coiled structure and effective medium*, **(d)** *Effective medium's refractive index vs. frequency response curve*

This coiled AEH structure example consists of an air waveguide with coiled cells of variable height. The structure results in a simplified effective medium with a nearly-constant high effective refractive index across the lower-frequency acoustic range of interest. Such a high refractive index response curve allows for effective AEH performance in a small footprint [27]. This design is effective at the expense of additional complexity.

While a multitude of AEH structure types exist, prior literature lacks adequate exploration regarding acoustic wave behavior in structures possessing geometric symmetry without uniform unit cells. Instead, the existing literature has focused either on geometries that lack complete geometric symmetry or on geometries that use uniform unit cells to achieve complete geometric symmetry. This study intended to investigate acoustic rainbow trapping behavior in a two-dimensional axisymmetric AEH structure. The investigation began with selecting the unit cell geometries and variations for use in the AEH prototype.

Chapter 3

Unit Cell Modeling

A Finite Element Method (FEM) approach was employed for this study. As part of this approach, acoustic wave trapping performance was modeled in COMSOL Multiphysics® v5.5 beginning with unidimensional unit cells. These unit cells are discrete functional components that can be repeated and varied in a pattern to form an entire acoustic energy harvesting structure. Unit cell geometry selection is a critical component of AEH design because each geometry produces a unique set of acoustic bandgap properties. These bandgap properties ultimately determine the AEH's ability to effectively use acoustic rainbow trapping to capture the frequencies of interest.

While a plethora of unit cell geometries are possible candidates for acoustic energy harvesting applications, five distinct unit cell geometries were evaluated:

1. Grooves with variable groove width;
2. Grooves with variable extrusion width;
3. Cylindrical pillars with variable diameter;
4. Holes with variable diameter; and
5. Cut-through holes with variable diameter.

Grooves [15], cylindrical pillars [7], and holes [24] are all featured in preexisting literature. However, the unit cell dimensions used in this study differed from the prior work found in literature. In an effort to ensure dimensional consistency while evaluating the five aforementioned 1D geometries, multiple variables were defined as immutable constants for each evaluated geometry. Table 1 specifies the constant control values of the variables used to evaluate the acoustic wave trapping capabilities of each 1D unit cell geometry.

Table 1

1D Unit Cell Geometry Configurations — Dimension Control Values

Dimension	Control Value
Unit Cell Height	4.000 mm
Unit Cell Length	5.650 mm
Groove/Pillar/Hole Depth	1.610 mm
Groove Width or Pillar/Hole Diameter	2.950 mm
Extrusion Width	2.700 mm
Plate Depth (for Pillars)	2.390 mm

These control values remained consistent for all five 1D unit cell geometries except in the case of dependent parameters. Each of the evaluated 1D geometries experienced iterative changes in one primary iterative parameter as well as up to one dependent parameter. For example, the two groove geometries varied either the groove width or extrusion width as the primary parameter while the other variable remained constant. This primary parameter variation resulted in a corresponding change to the overall unit cell length since all other variables were held constant. For any given unit cell within a grooved geometry (n), the overall unit cell length (Λ_n) is the sum of the groove width (w_n) and the extrusion

width (s_n), as illustrated in Equation 7.

$$\Lambda_n = w_n + s_n \tag{7}$$

In this case, the unit cell length was a parameter dependent upon the value of the groove width, treated as either a constant or as a primary iterative parameter, as well as the extrusion width, also treated as either a constant or as a primary iterative parameter. Table 2 specifies the primary iterative parameters as well as any relevant dependent parameters associated with each of the five evaluated 1D geometries.

Table 2

1D Unit Cell Geometry Configurations — Primary and Dependent Parameters

Geometry	Lower-Range	Mid-Point	Upper-Range
1: Grooves –	Unit Cell Length = 5.15 mm	Unit Cell Length = 5.65 mm	Unit Cell Length = 6.15 mm
Variable Groove Width	Groove Width = 2.45 mm	Groove Width = 2.95 mm	Groove Width = 3.45 mm
2: Grooves –	Unit Cell Length = 5.650 mm	Unit Cell Length = 6.800 mm	Unit Cell Length = 7.950 mm
Variable Extrusion Width	Extrusion Width = 2.700 mm	Extrusion Width = 3.850 mm	Extrusion Width = 5.000 mm
3: Pillars – Variable Diameter	Pillar Diameter = 2.700 mm	Pillar Diameter = 3.850 mm	Pillar Diameter = 5.000 mm
4: Holes – Variable Diameter	Hole Diameter = 2.700 mm	Hole Diameter = 3.850 mm	Hole Diameter = 5.000 mm
5: Through Holes – Var. Dia.	Hole Diameter = 2.700 mm	Hole Diameter = 3.850 mm	Hole Diameter = 5.000 mm

3.1 Grooves — Variable Groove Width

The first 1D unit cell geometry evaluated as part of this study was a unit cell with grooves of variable groove width. Grooves were evaluated for several reasons including:

1. Geometric simplicity;
2. Ease of manufacturing;
3. Relative adaptability to differing dimensions; and
4. Large amount of prior work relating to groove-based energy harvesting structures.

Since the initial 1D unit cell analysis intentionally constrained both feature depth and overall unit cell height, feature width and overall unit cell width were left as free variables. To effectively evaluate the effect of a grooved unit cell's overall width on the unit cell geometry's acoustic wave trapping performance, the groove width was varied while holding the extrusion width at a constant value. Figure 9 illustrates the three geometric configurations evaluated for grooves of variable groove width.

Figure 9

Grooves — Variable Groove Width Geometries

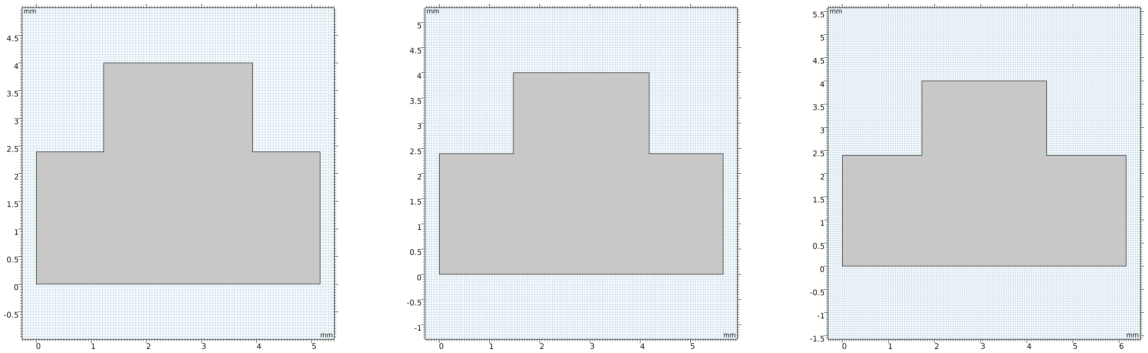

(a) *Lower-Range: Groove Width = 2.450 mm*

(b) *Mid-Point: Groove Width = 2.950 mm*

(c) *Upper-Range: Groove Width = 3.450 mm*

3.2 Grooves — Variable Extrusion Width

After evaluating grooves of variable groove width, evaluating the acoustic wave trapping performance of grooves of variable extrusion width was the next logical step. Similar to the case of grooves of variable groove width, the grooves of variable extrusion width evaluation involved varying only the unit cell's extrusion width while holding the groove width as a constant. Figure 10 illustrates the three geometric configurations evaluated for grooves of variable extrusion width.

Figure 10

Grooves — Variable Extrusion Width Geometries

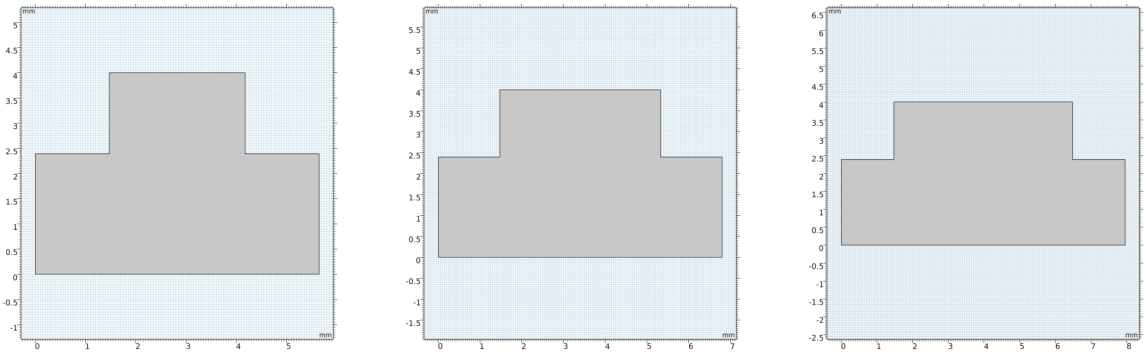

(a) *Lower-Range: Extrusion Width = 2.700 mm*

(b) *Mid-Point: Extrusion Width = 3.850 mm*

(c) *Upper-Range: Extrusion Width = 5.000 mm*

3.3 Cylindrical Pillars — Variable Diameter

Following the evaluation of grooves of variable extrusion width, cylindrical pillars of variable diameter were next evaluated. Cylindrical pillars are also adaptable to differing dimensions, but such pillars are typically more difficult to manufacture than simple grooves. These 1D unit cells solely varied the pillar diameter while holding all other param-

eters at a constant value. Figure 11 illustrates the three geometric configurations evaluated for cylindrical pillars of variable diameter.

Figure 11

Cylindrical Pillars — Variable Diameter Geometries

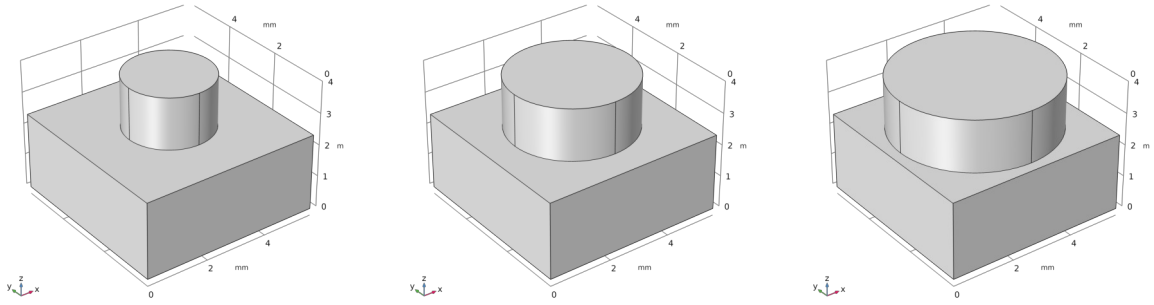

(a) *Lower-Range: Diameter = 2.700 mm*

(b) *Mid-Point: Diameter = 3.850 mm*

(c) *Upper-Range: Diameter = 5.000 mm*

3.4 Holes — Variable Diameter

Holes of variable diameter were next evaluated. Holes are essentially inverted pillars, but this study intended to evaluate the differences in acoustic wave trapping performance between similarly sized holes and pillars. Similar to cylindrical pillars, these holes were varied only in their diameter while leaving all other parameters at a constant value. Figure 12 illustrates the three geometric configurations evaluated for cylindrical holes of variable diameter.

Figure 12

Cylindrical Holes — Variable Diameter Geometries

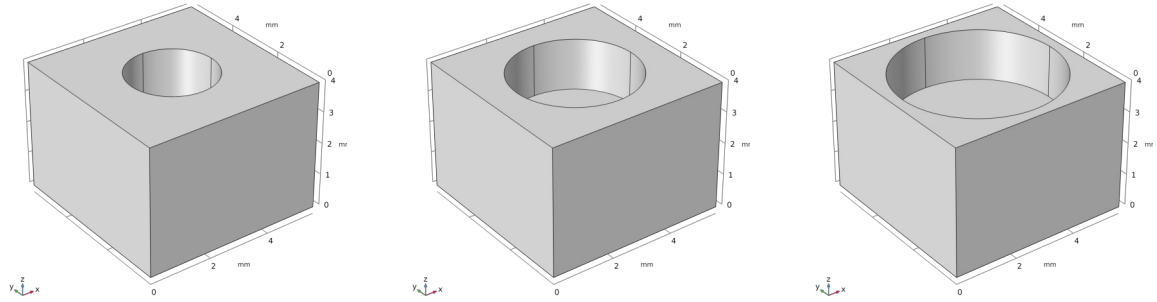

(a) *Lower-Range: Diameter = 2.700 mm*

(b) *Mid-Point: Diameter = 3.850 mm*

(c) *Upper-Range: Diameter = 5.000 mm*

3.5 Through Holes — Variable Diameter

Lastly, through holes of variable diameter were evaluated. Through holes are holes that extend completely through the 1D unit cell instead of having a limited depth to match the feature depth of the other 1D unit cells. While through holes are similar to holes with fixed depth, this study intended to evaluate the difference in acoustic wave trapping performance between these two unit cell geometries. Figure 13 illustrates the three geometric configurations evaluated for cylindrical through holes of variable diameter.

Figure 13

Cylindrical Through Holes — Variable Diameter Geometries

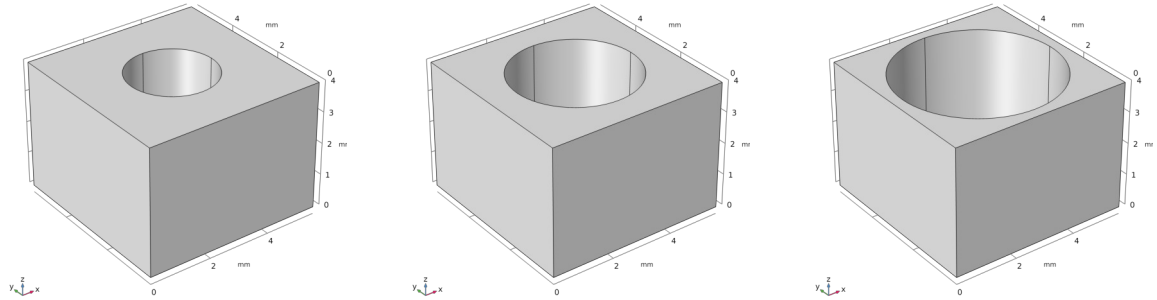

(a) *Lower-Range: Diameter = 2.700 mm*

(b) *Mid-Point: Diameter = 3.850 mm*

(c) *Upper-Range: Diameter = 5.000 mm*

3.6 1D Unit Cell Geometry Comparison

The COMSOL Multiphysics® simulation results for each of the 1D unit cell geometries were evaluated with respect to their demonstrated acoustic band gaps. Such band gaps are indicated by spaces between acoustic frequency response curves for a given acoustic structure. These acoustic frequency response curves represent individual acoustic propagation modes for acoustic waves traveling through an acoustic structure. Band gaps appear for frequencies where the acoustic structure blocks propagation of acoustic waves.

Since a wider band gap allows for a greater potential capture of environmental acoustic waves, optimizing the AEH's acoustic energy capture performance relied heavily on maximizing the band gap exhibited in the selected 1D unit cell geometry. Figure 14 illustrates the acoustic band gaps observed for the aforementioned 1D unit cell geometries.

Figure 14

1D Unit Cell Geometries - Acoustic Band Gap Comparison

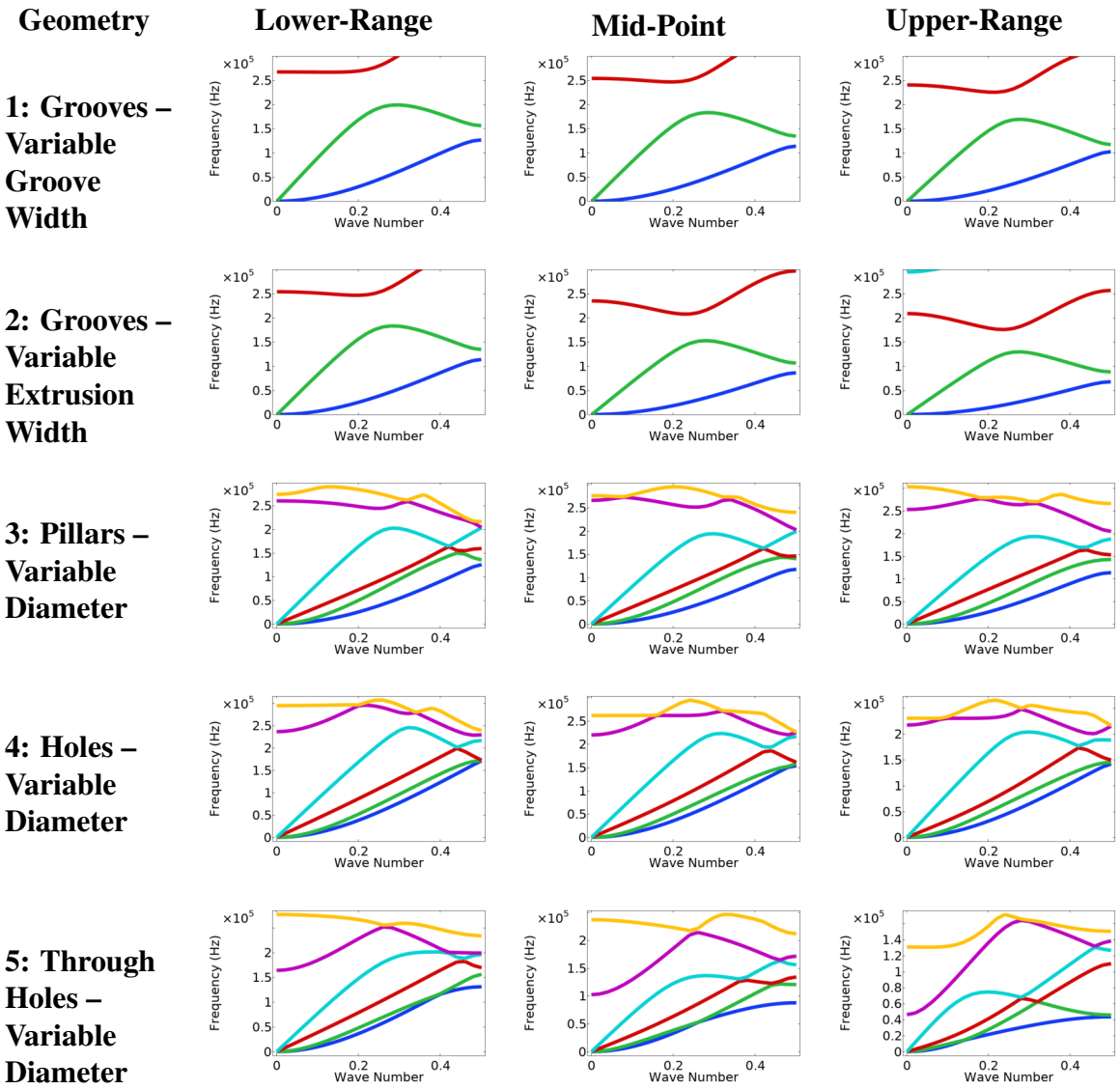

These frequency response curves illustrate distinct acoustodynamic differences between the evaluated 1D unit cell geometries. Multiple acoustic wave propagation modes exist for each evaluated geometry, but pillar- and hole-based geometries exhibited greater numbers of propagation modes compared to grooved geometries. The additional acoustic wave propagation modes present for these geometries result in a more complex situation

where there is more competition for finite frequency space between individual propagation modes. This leads to reduced band gaps between the individual frequency response curves compared to grooved geometries. Furthermore, the fewer acoustic propagation modes present in the grooved geometries imply that such structures are more easily excited compared to the other evaluated geometries. Greater structural excitation generally allows for easier physical measurement collection.

As is illustrated by the frequency response curves, grooves of variable extrusion width exhibited the largest consistent band gaps between the second (green curve) and third (red curve) acoustic propagation modes. These results indicated that grooves of variable extrusion width would be the most promising 1D unit cell geometry for further optimization and subsequent use in an AEH prototype.

3.7 Grooves — Variable Groove/Plate Depth Ratio

As is illustrated by the band gaps displayed in the frequency response curves in Figure 14, both grooved geometries demonstrated superior band gaps compared to the competing geometries. While both grooved geometries demonstrated wide and clear band gaps, each of the competing geometries demonstrated smaller and less clearly-defined band gaps. Either grooved geometry would have served well for an AEH application, but grooves of variable extrusion width offered slightly improved acoustic wave capture performance compared to their variable groove width counterparts.

After determining that grooves of variable extrusion width offered the best potential acoustic wave trapping performance across the frequency range of interest, it was necessary to next evaluate the effect of groove depth on wave trapping performance. The previous 1D unit cell geometries specifically held feature depths such as groove depth at a constant value to ensure results comparability. This study also evaluated the relationship between the ratio of groove depth and plate depth with respect to acoustic wave trapping performance. Table 3 lists the evaluated configurations for grooves of variable groove depth.

Table 3

Grooves — Evaluated Groove Depth / Plate Depth Ratios — Constant Plate Depth

Groove Depth (mm)	Plate Depth (mm)	GD/PD Ratio (%)
1.010	4.000	25.25
1.210	4.000	30.25
1.410	4.000	35.25
1.610	4.000	40.25
1.810	4.000	45.25
2.010	4.000	50.25
2.210	4.000	55.25
2.410	4.000	60.25
2.610	4.000	65.25

Figure 15 illustrates the acoustic frequency response curves for these nine evaluated configurations resulting in an optimal groove/plate depth ratio of 40.25%.

Figure 15

Grooves — Variable Groove/Plate Depth Ratio — Acoustic Band Gap Comparison

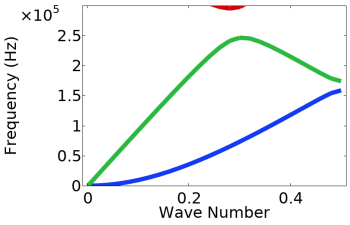

(a) *Grooves – Var. Groove Depth* ***Groove Depth = 1.010 mm***

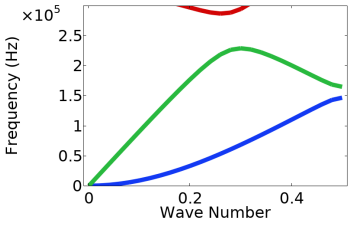

(b) *Grooves – Var. Groove Depth* ***Groove Depth = 1.210 mm***

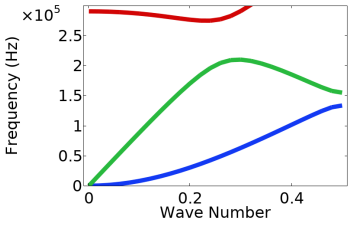

(c) *Grooves – Var. Groove Depth* ***Groove Depth = 1.410 mm***

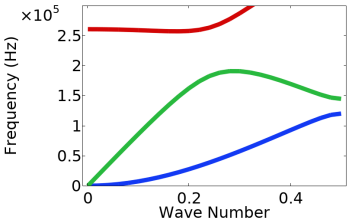

(d) *Grooves – Var. Groove Depth* ***Groove Depth = 1.610 mm***

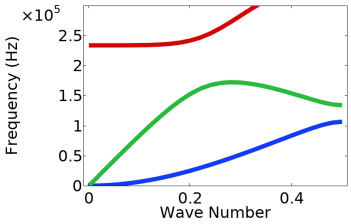

(e) *Grooves – Var. Groove Depth* ***Groove Depth = 1.810 mm***

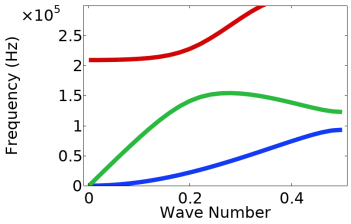

(f) *Grooves – Var. Groove Depth* ***Groove Depth = 2.010 mm***

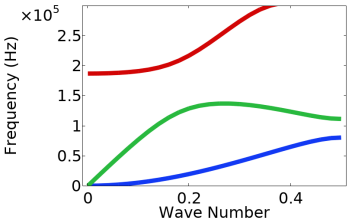

(g) *Grooves – Var. Groove Depth* ***Groove Depth = 2.210 mm***

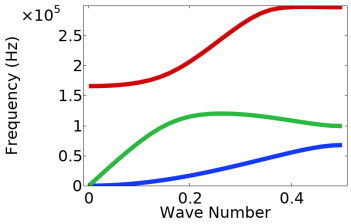

(h) *Grooves – Var. Groove Depth* ***Groove Depth = 2.410 mm***

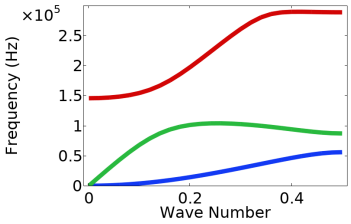

(i) *Grooves – Var. Groove Depth* ***Groove Depth = 2.610 mm***

3.8 Grooves — Constant Groove / Plate Depth Ratio

After determining the optimal groove depth to plate depth ratio of 40.25%, it was necessary to evaluate the performance of different groove depths while maintaining this groove/plate depth ratio. Plate depth is the primary concern since it dictates the thickness of the material used in the physical AEH structure. Table 4 lists the observed band gaps across varying plate and groove depths with a constant 40.25% groove / plate depth ratio.

Table 4

Band Gaps — Grooves — Constant Groove / Plate Depth Ratio

Plate Depth (mm)	**Groove Depth (mm)**	**GD/PT Ratio (%)**	**Band Gap (10^5 Hz)**
2.000	0.805	40.25	0.50
2.500	1.006	40.25	0.60
3.000	1.208	40.25	0.65
3.500	1.409	40.25	0.70
4.000	1.610	40.25	0.65
4.500	1.811	40.25	0.50
5.000	2.013	40.25	0.35
5.500	2.214	40.25	0.25
6.000	2.415	40.25	0.05

Figure 16 illustrates the acoustic frequency response curves for these nine evaluated configurations.

Figure 16

Grooves — Constant Groove/Plate Depth Ratio — Acoustic Band Gap Comparison

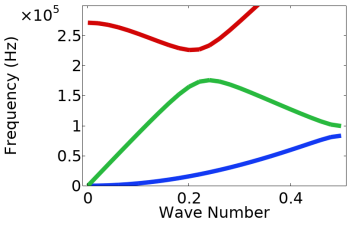

(a) *Grooves – Constant Groove/Plate Depth Ratio* ***Plate Depth = 2.000 mm***

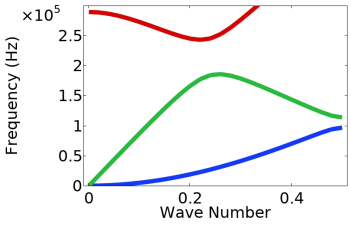

(b) *Grooves – Constant Groove/Plate Depth Ratio* ***Plate Depth = 2.500 mm***

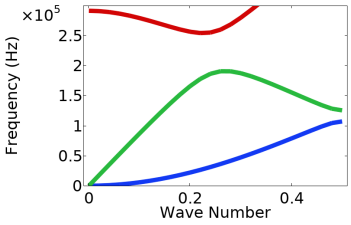

(c) *Grooves – Constant Groove/Plate Depth Ratio* ***Plate Depth = 3.000 mm***

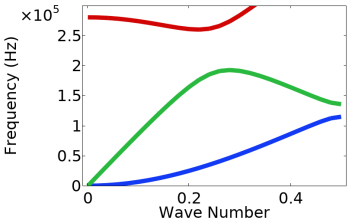

(d) *Grooves – Constant Groove/Plate Depth Ratio* ***Plate Depth = 3.500 mm***

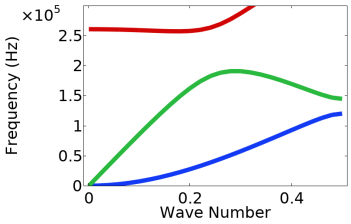

(e) *Grooves – Constant Groove/Plate Depth Ratio* ***Plate Depth = 4.000 mm***

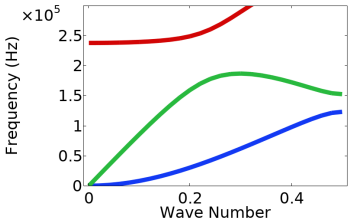

(f) *Grooves – Constant Groove/Plate Depth Ratio* ***Plate Depth = 4.500 mm***

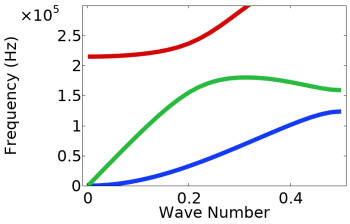

(g) *Grooves – Constant Groove/Plate Depth Ratio* ***Plate Depth = 5.000 mm***

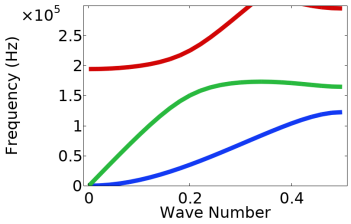

(h) *Grooves – Constant Groove/Plate Depth Ratio* ***Plate Depth = 5.500 mm***

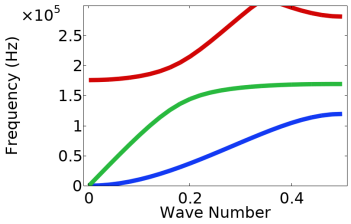

(i) *Grooves – Constant Groove/Plate Depth Ratio* ***Plate Depth = 6.000 mm***

This analysis indicated that the optimal plate depth for the fixed 40.25% groove / plate depth ratio ranged between 3.000 mm and 4.000 mm. A 3.175 mm thick plate (1/4 in.) was selected due to this thickness falling within the optimal plate depth range as well as its ease of material sourcing. Aluminum 6061-T6 plates of 3.175 mm depth are quite commonly available while meeting the specifications required by the AEH design, and this material proved convenient for manufacturing the AEH prototype. The optimized final 1D unit cell dimensions for grooves of variable extrusion width are listed in Table 5. The entire

AEH prototype structure is comprised of an array of 1D unit cells with these specifications.

Table 5

Grooves — Final 1D Unit Cell Dimensions

Dimension	**Value**
Plate Depth	3.175 mm
Groove Depth	1.270 mm
Plate / Groove Depth Ratio	40.00%
Groove Width	2.700 mm
Extrusion Width	2.000 mm - 3.650 mm
Unit Cell Length	4.700 mm - 6.350 mm

Chapter 4

2D Axisymmetric Disc Modeling

Following the determination of the optimal AEH 1D unit cell parameters, the next step in the AEH development process involved designing an acoustic trapping pattern comprised of an array of these 1D unit cells. This acoustic trapping pattern was then transformed into a 2D axisymmetric AEH disc simulation using COMSOL Multiphysics®. This chapter discusses the design, modeling, and optimization process for the 2D axisymmetric AEH disc in preparation for physical prototyping and results validation.

4.1 Modeling Configuration

4.1.1 Physical Parameter Selection

While a variety of 1D unit cell parameters would have been suitable for the 100 kHz to 220 kHz frequency range of interest, the exact AEH disc dimensions were selected with consideration to physical fabrication limits. For example, the CNC milling machine available for this project's use could only accommodate a material size up to 18 in. x 18 in. x 18 in. (457.2 mm x 457.2 mm x 457.2 mm). This limited the 2D AEH disc design to a maximum diameter of 18 in. (457.2 mm). Furthermore, the OMAX abrasive waterjet cutter available for this project's use could only accommodate a material size up to 24 in. x 24 in. x 1 in. (609.6 mm x 609.6 mm x 25.4 mm). This limited the size of aluminum sheeting used in fabrication.

Moreover, 6061-T6 aluminum sheets of this size are most commonly available in thickness increments of 1/8 in. (3.175 mm). For ease of fabrication and testing while maintaining high acoustic energy capturing ability, 24 in. x 24 in. x 1/8 in. (609.6 mm x 609.6 mm x 3.175 mm) 6061-T6 aluminum sheets were selected for the final AEH disc prototype. The 2D axisymmetric AEH disc was designed in SolidWorks® and modeled in COMSOL Multiphysics® specifically taking these final dimensions into consideration.

4.1.2 2D Side Profile — Circular Revolution

Since this AEH disc was intended to be completely axisymmetric, designing a 2D side profile and revolving it in a complete circle appeared to be the most efficient and precise development method. The axisymmetric nature of this design guarantees that all locations along the AEH disc at a given radial distance will all share the same exact physical feature dimensions.

This 2D side profile includes an array of 34 AEH unit cells with constant groove width of 2.70 mm, groove depth of 1.27 mm from the top surface of the AEH disc, and extrusion widths linearly increasing from 2.00 mm to 3.65 mm along the radial dimension of the AEH disc. Figure 17 illustrates the 2D axisymmetric AEH disc's side profile.

Figure 17

2D Axisymmetric AEH Disc — Side Profile

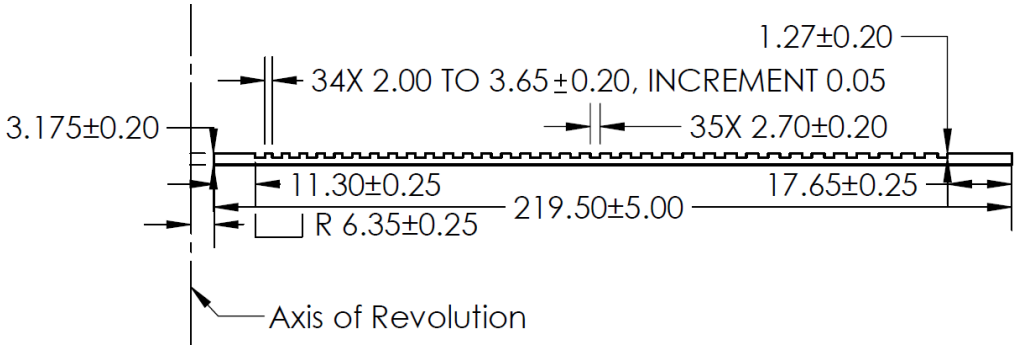

To facilitate the fabrication process, the AEH disc features a 0.5 in. (12.7 mm) diameter hole in its center for use with a through clamp. Including this center hole, the AEH disc has an overall diameter of 17.78 in. (451.7 mm). The first unit cell begins at 11.30 mm from the outer edge of this center hole, or 17.65 mm from the center of the AEH disc. The last unit cell ends at a radial distance of 17.65 mm from the outer edge of the

AEH disc. As previously indicated, the AEH disc's overall thickness is 1/8 in. (3.175 mm).

4.1.3 COMSOL Multiphysics® Settings

As is the case with many simulation packages, COMSOL Multiphysics® offers multiple options for simulating any given geometry. This type of AEH disc may be effectively simulated as a:

1. 3D solid component; or
2. 2D axisymmetric component.

Axisymmetry assumes that a given structure is symmetrical with respect to a given axis. The AEH harvester disc used in this study was specifically designed to fulfill the requirements for an axisymmetric analysis. The grooved disc structure is designed to be perfectly symmetrical around its center vertical axis (Z-axis) so that waves also propagate symmetrically with respect to this axis. Furthermore, the center-mounted piezoelectric actuator also fulfills the axisymmetric conditions since it is circular with the same Z-axis shared with the AEH disc structure. Likewise, waves produced by the center piezoelectric actuator propagate throughout the actuator and AEH disc structure in a symmetric pattern with respect to the shared Z-axis.

This condition is particularly useful because a 3D FEA analysis can be significantly more computationally and analytically intensive compared to a 2D FEA analysis. In a 2D analysis, waves are trapped at different distances in only one direction. However, a 3D analysis of a sufficiently thin structure results in waves being trapped in two directions. An axisymmetric condition essentially translates the expected 2D analysis results into a 3D disc where distance from the structure's center predicts the acoustic wave trapping behavior. In this case, acoustic waves are trapped along the concentric grooves cut into the AEH disc structure. Such behavior is similar to the results obtained from a 2D analysis, and this significantly simplifies the acoustic wave rainbow trapping performance analysis.

Modeling a disc as a 3D component is the conventional option. It relies on either importing a 3D CAD model from another CAD application or defining the structure completely within COMSOL Multiphysics®. Either method is acceptable, but this project used a separately-drawn 2D side profile that could also be circularly revolved within SolidWorks® to produce the entire 3D disc structure. This disc was then imported into COMSOL Multiphysics® for evaluation. However, this method is quite computationally intensive since COMSOL Multiphysics® attempts to apply an automated FEA solver to each element within the model mesh. This mesh is unique for each physical location within the disc structure, so the software is unable to effectively repeat any results from other parts of the disc structure. This leads to significant redundancy in the computational load along with the associated increase in computation time.

Conversely, modeling this AEH disc as a 2D axisymmetric model within COMSOL Multiphysics® offers several advantages. Firstly, it provides a simplified configuration process since the 2D side profile can be imported directly into COMSOL Multiphysics® from a DXF file. Such DXF files are easily exported from nearly any popular CAD application. COMSOL Multiphysics® is then able to revolve the provided 2D side profile into a circular disc, and it applies the 2D axisymmetric conditions to the resulting disc. This allows COMSOL Multiphysics® to assume symmetry around the disc's central axis of revolution, and this symmetry condition avoids redundant mesh calculations that were experienced with the 3D component method. The primary advantage is saving a significant amount of time for computation. For example, a given workstation took over 24 hours to fully compute an AEH analysis using the 3D component option. The same workstation took under seven seconds to complete the same AEH analysis using the 2D axisymmetric component option. Furthermore, the 2D axisymmetric component option allows for greater certainty regarding the structure's symmetry since symmetry is guaranteed by this analysis mode. With the 3D component option, there is a small chance that the resulting 3D structure is not treated as being completely symmetrical as designed due to mesh element geometry variations and

the resulting propagation throughout the FEA solver workflow.

4.1.4 Boundary Conditions

Boundary conditions are critical for any type of FEA simulation because they define how the entire simulation will operate. The 2D axisymmetric AEH disc modeled in COMSOL Multiphysics® relied on three main boundary condition assignments:

1. Boundary load (-10 N/m^2) at the left side of the top surface of the AEH disc;
2. Low-reflection boundary around the outer perimeter of the AEH disc; and
3. Free boundary on the remaining surfaces of the AEH disc.

The -10 N/m^2 boundary load was applied on the top surface of the AEH disc between r = 0 mm and r = 3.65 mm to simulate the vibration input excitation from a piezoelectric actuator. A low-reflection boundary was applied to the outer perimeter of the AEH disc to reduce internal reflections within the AEH disc structure. Without this boundary condition, waves reaching the outer perimeter of the disc would tend to propagate back through the disc towards the direction from which they originated. This would cause an undesirable condition making it more difficult to distinguish between incident waves and internally reflected waves. Lastly, a default free space boundary was applied to all remaining surfaces to minimize any sort of external interference with the acoustic trapping simulation results.

In addition to these boundary conditions, the 2D axisymmetric component option automatically assigns an Axial Symmetry condition to the leftmost portion of the imported 2D side profile. This condition is required as part of the 2D axisymmetric simulation mode, and the condition mandates direct contact between the axis of revolution and a boundary on the component's geometry. As such, the center hole could not be directly modeled using the imported 2D side profile since the Axial Symmetry boundary would be floating in free space. With the Axial Symmetry boundary in direct contact with the first part of the disc's geometry, the center hole was not displayed. This was resolved by entering an R = -6.35

mm offset value within the Revolution 2D results parameters to incorporate the center hole within the resulting disc structure.

4.2 Acoustic Wave Trapping — Modeling Calculations and Plots

Acoustic energy harvesting performance can be predicted through various means. Fundamentally, an acoustic wave's vibrations cause physical displacement, stress, and strain within their carrier medium. In this scenario, the aluminum structure of the AEH disc will be subjected to these forces by any acoustic waves propagating through the AEH.

One particularly useful method of analyzing acoustic wave trapping performance in the simulated AEH disc structure is defining a cut line across the AEH disc structure then plotting the frequency response curves for different frequencies along the cut line. In this case, the cut line is configured to span the entire radius of the AEH disc structure cross-section at half of the structure's 3.175 mm total height (1.5875 mm). This allows for acoustic wave trapping performance evaluation across the entire diameter of the AEH disc structure while focusing on wave propagation at the bottom edge of the grooves. The red line in Figure 18 illustrates the acoustic wave analysis cut line across the simulated AEH disc structure.

Figure 18

2D Axisymmetric AEH Disc Simulation — Cross-Sectional Energy Analysis Cut Line

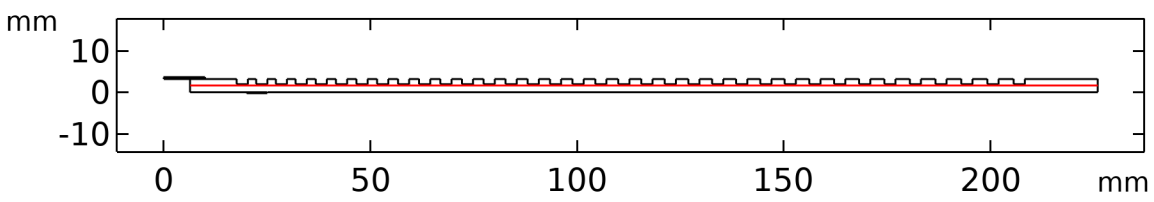

Using this defined cut line, the simulated AEH disc structure's acoustic wave trap-

ping performance at varying locations is plotted for specified frequencies of interest. Figure 19 illustrates the acoustic wave trapping performance of 165 kHz, 190 kHz, and 215 kHz waves at various radial distances (arc lengths) across the simulated AEH disc structure.

Figure 19

2D Axisymmetric AEH Disc Simulation — Cross-Sectional Energy

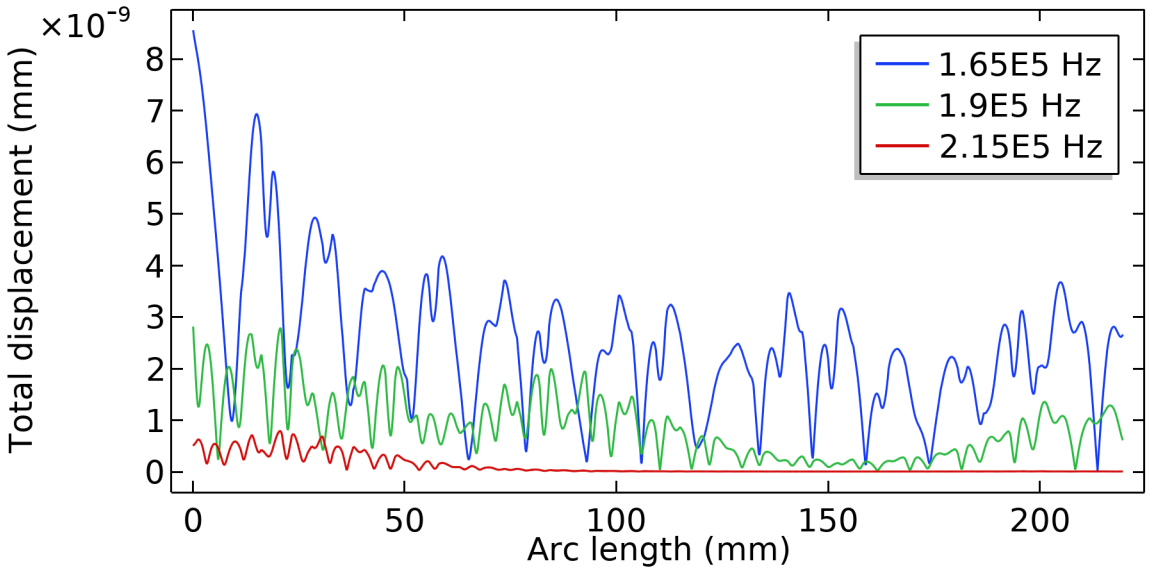

COMSOL Multiphysics® conveniently offers both a 2D displacement plot as well as a 3D stress plot for evaluating the AEH disc's acoustic wave trapping performance. The 2D displacement is correlated with the concentration of acoustic waves captured along the AEH disc's structure, and the 3D von Mises stress offers an indicator of the energy capture potential along the AEH disc's structure. The 2D displacement and 3D stress were analyzed using separate plots generated in 5 kHz intervals for the frequencies of interest ranging from 100 kHz to 220 kHz. Figure 20 and Figure 21 illustrate some of the 2D axisymmetric AEH disc simulation results for 2D displacement and 3D stress, respectively.

Figure 20

2D Axisymmetric AEH Disc Simulation — 2D Displacement

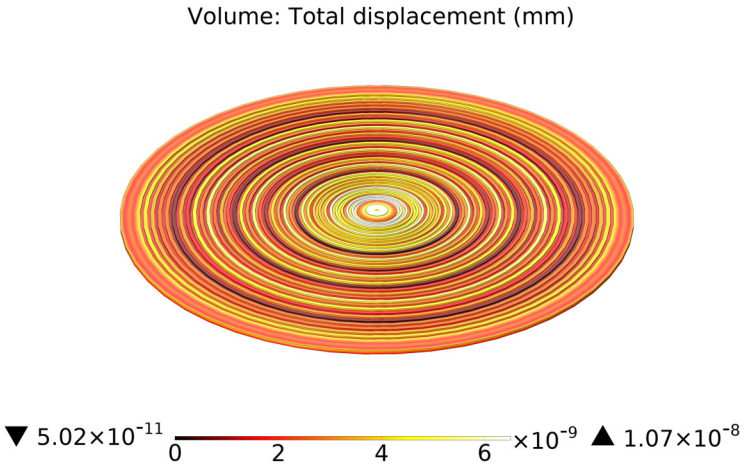

(a) *Frequency = 165 kHz*

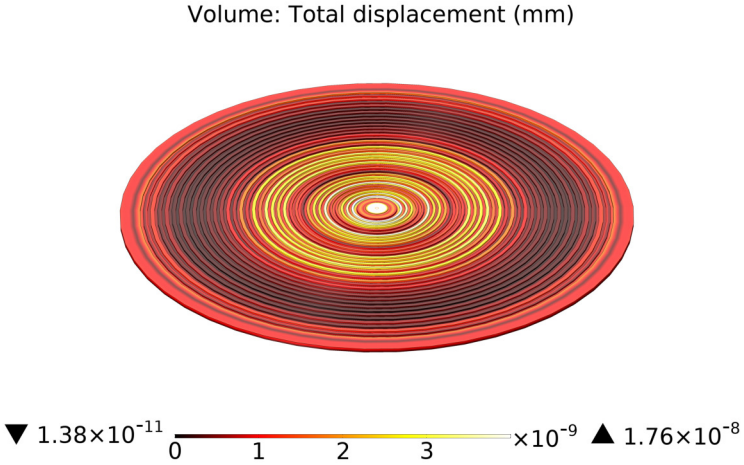

(b) *Frequency = 190 kHz*

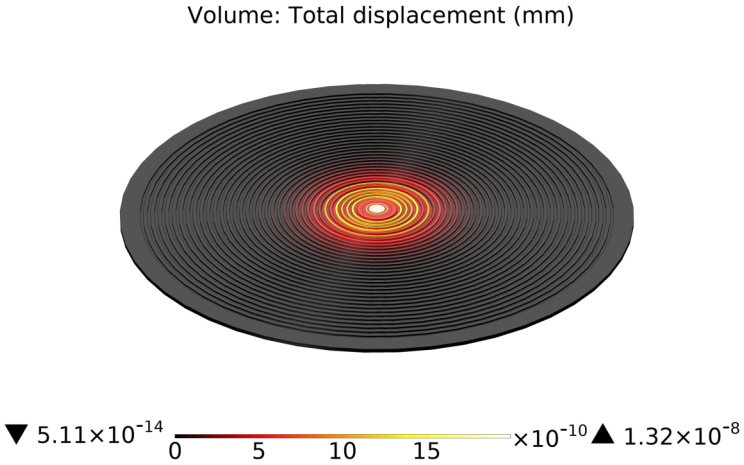

(c) *Frequency = 215 kHz*

Figure 21

2D Axisymmetric AEH Disc Simulation — 3D Stress

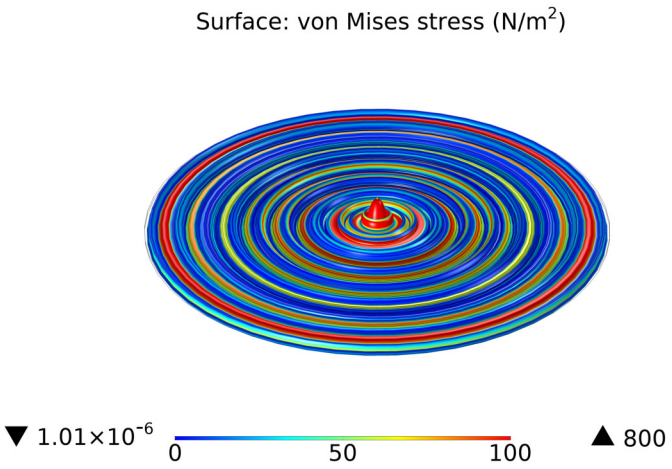

(a) *Frequency = 165 kHz*

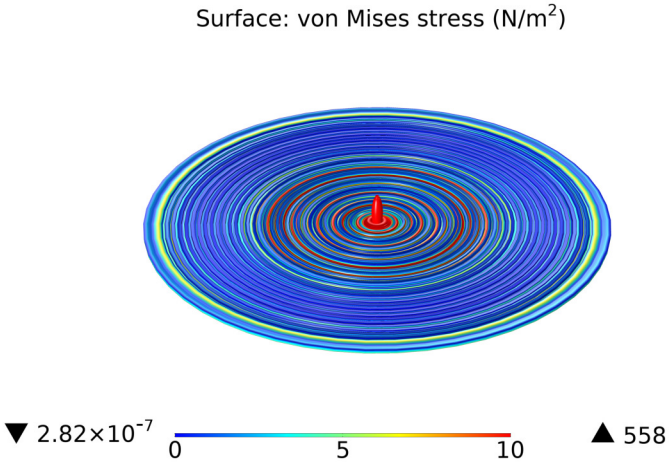

(b) *Frequency = 190 kHz*

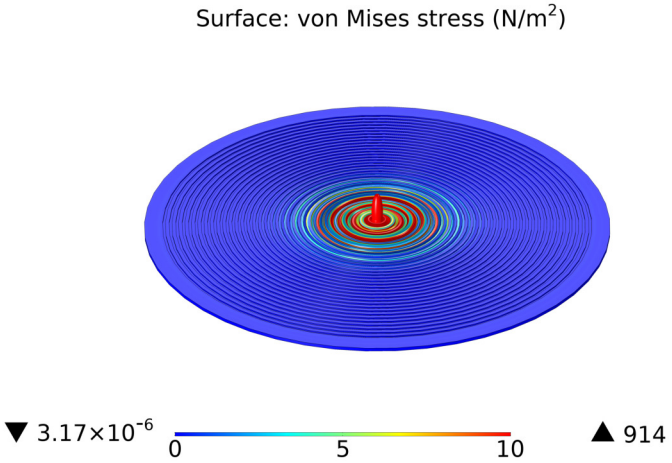

(c) *Frequency = 215 kHz*

Both the 2D displacement and 3D stress plots illustrate similar trends. Areas of the AEH disc closer to the center tend to have higher rates of acoustic trapping at higher frequencies, whereas areas closer to the outer perimeter of the AEH disc tend to display higher excitation from lower frequencies. As defined by Equation 8, this behavior is expected due to the inversely proportional relationship of a sinusoidal wave's wavelength to its frequency.

$$\lambda = \frac{v}{f} \tag{8}$$

Equation 8 illustrates that a wave's wavelength (λ) is equal to its phase speed (v) divided by its frequency (f). While the phase speed may vary due to material differences, sinusoidal waves of higher frequency correspond to shorter wavelengths. Shorter wavelengths cause waves to be trapped more easily towards the center of the AEH disc where extrusion widths are also shorter. Conversely, longer wavelengths are able to propagate throughout the AEH disc structure until they reach a suitably matched extrusion width within the AEH disc.

If a given wave is not trapped by the physical AEH disc structure by the time it reaches the AEH disc's outer perimeter, it may internally reflect until it expends enough energy to settle within the AEH disc structure. Alternatively, such a wave may also escape the confines of the AEH disc altogether and continue traveling through air or whatever other medium borders the AEH disc structure. While it is somewhat difficult to directly measure the rate of energy loss due to waves internally reflecting or escaping the confines of the AEH disc structure, overall AEH wave capture efficiency is more easily determined by examining the waves that are trapped within the AEH disc structure. These simulation results were then validated through the fabrication and evaluation of a physical prototype.

Chapter 5

Physical Prototype Fabrication

After completing the 2D axisymmetric disc modeling in COMSOL Multiphysics®, the next step in the AEH development process was to validate the design with a physical prototype. The physical prototype fabrication process involved the following steps:

1. Procuring required materials;
2. Preparing a 3D CAD model;
3. Cutting the overall disc shape using an abrasive waterjet cutting machine;
4. Machining the acoustic trapping grooves using a CNC milling machine; and
5. Assembling and attaching piezoelectric sensors to the AEH disc.

5.1 Fabrication Materials

Fabricating the physical prototype required several materials ranging from aluminum sheets to quick-setting epoxy adhesives. These are all readily available materials, and various modifications were performed during the fabrication process. While most of these materials were easily procured from mainstream vendors such as online megastores and sheet metal distributors, the particular piezoelectric devices used were purchased from a specialty vendor. The piezoelectric sensors were specifically selected due to their small diameter (5 mm) allowing for improved physical signal isolation and their resonance frequency (200 kHz) closely matching the frequency range of interest (100-220 kHz). Table 6 lists the materials used during the fabrication process for the physical acoustic energy harvester disc prototype.

Table 6

Physical AEH Prototype — Materials Used

z

Material	Quantity
6061-T6 Aluminum Sheets (610 mm x 610 mm x 3.175 mm)	1
Piezoelectric Actuators (35 mm diameter)	1
Piezoelectric Sensors (5 mm diameter)	9
Stranded Wire (32 AWG)	3 m
Electronics Wire Connectors	40
J-B Weld ClearWeld Quick-Setting Epoxy	2.5 mL

5.2 3D CAD Model

While the 2D axisymmetric disc modeling in COMSOL Multiphysics® relied on a side profile of the AEH design (Figure 17) that was revolved in a complete circle solely during the computational FEA process, this model was not immediately useful for physical machining purposes. However, it was trivial to create an entire 3D AEH disc structure within SolidWorks® using this same process of revolving the 2D side profile in a complete circular path. Figure 22 depicts the 3D CAD model used for the fabricated AEH disc.

Figure 22

Fabricated AEH Disc — 3D CAD Model

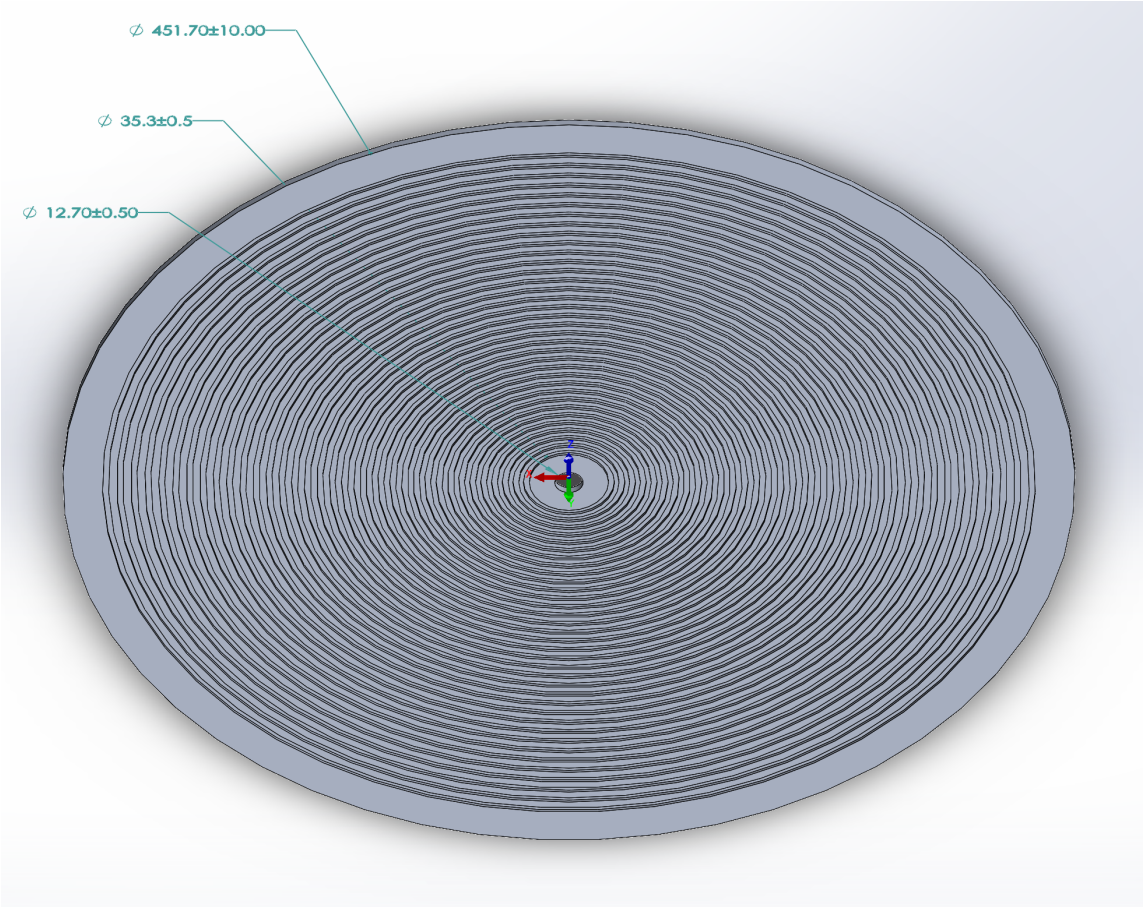

5.3 Waterjet Cutting

Abrasive waterjet cutting machines rely on 2D vector CAD files since such machines only operate in 2D coordinate space. The bottom view of the 3D SolidWorks® CAD model was easily exported as an AutoCAD® DXF (Drawing Interchange Format) file for importation into the OMAX waterjet cutter's proprietary CAM software. This DXF file contains only the outlines for the outer perimeter of the AEH disc as well as the perimeter of the AEH disc's center hole. Refer to Figure A1 for a waterjet cutting drawing featuring the outer disc and center hole cutting paths for the final 2D axisymmetric AEH disc.

The AEH disc blank was cut from a flat sheet of 6061-T6 aluminum using the OMAX waterjet cutter's default recommended cutting settings for aluminum material. After the waterjet cutting process was completed, any present machining burrs were removed by manually passing a deburring stone over the affected edges of the AEH disc blank. This process resulted in a high-quality machining blank for further machining of the AEH grooves using a CNC milling machine.

5.4 CNC Machining

While the original 2D axisymmetric AEH disc design did not feature a center hole, a 0.5 in (12.7 mm) hole was added in the center to aid the CNC machining process. CNC milling or turning of circular features such as the AEH grooves has the potential to result in undesirable vibrations, also known as chatter, during the machining process. Similar to playing a warped phonograph record, such vibrations often cause material distortions throughout the disc [28]. These material distortions may result in a final disc containing bent material or jagged grooves. To prevent chatter during the groove machining process, a clamp was attached to the AEH disc blank through its center hole. Additional clamps secured the outer surface of the AEH disc blank for the duration of the CNC milling process.

Refer to Figure A2 for a complete machining drawing for the final 2D axisymmetric AEH disc. The left side of the drawing features a top view of the energy harvester disc, and the right side of the drawing illustrates a revolved side profile view.

5.5 Piezoelectric Sensor Assembly & Attachment

The physical AEH disc prototype uses one 35 mm diameter center piezoelectric actuator to transmit input frequencies to the AEH disc in conjunction with an array of 5 mm diameter piezoelectric sensors to measure the frequency response at various locations across the bottom of the AEH disc structure. Figure 23 illustrates the overall testing configuration for the physical AEH prototype.

Figure 23

Physical AEH - Testing Configuration Overview

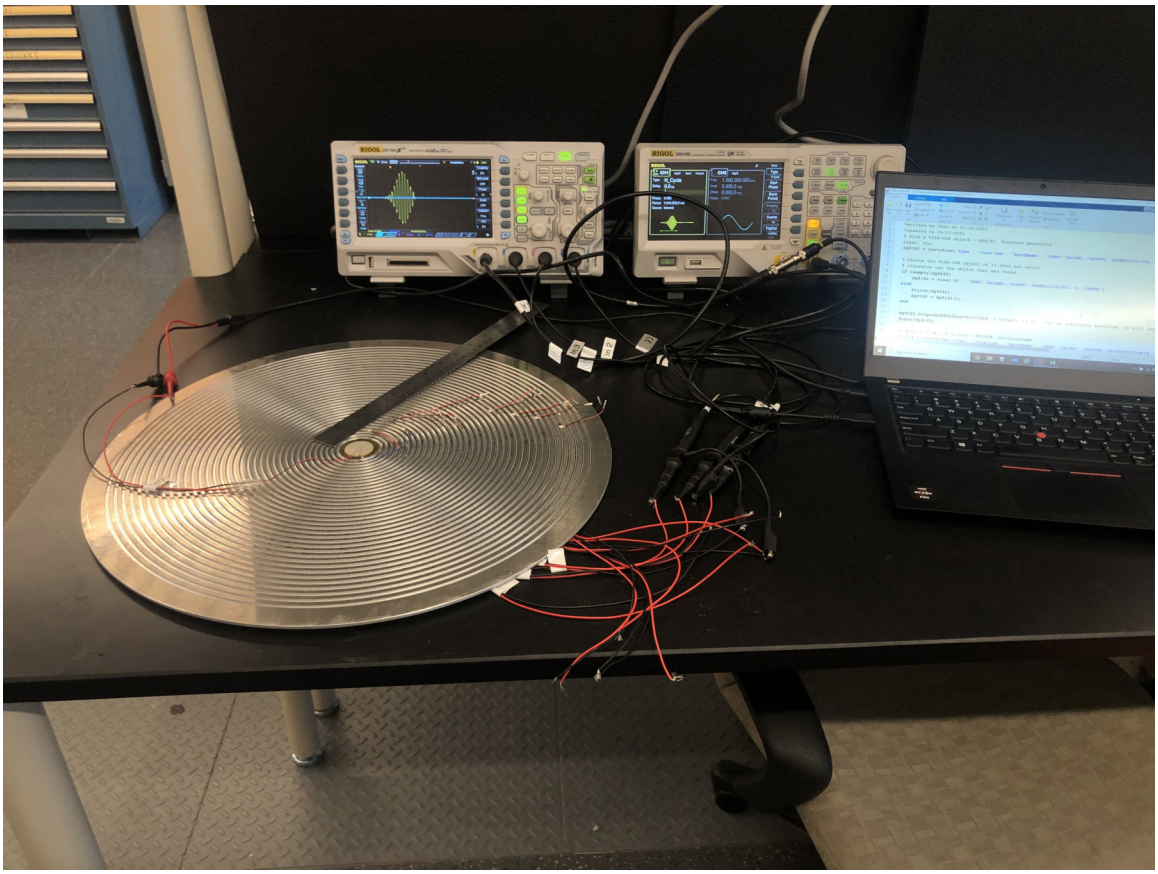

Note. The 5 mm piezoelectric sensors attached to the top surface of the AEH disc in this figure were only used for evaluation purposes and not for gathering the final frequency response data.

The testing apparatus consisted of the following components:

1. One (1) RIGOL DG4162 function/arbitrary waveform generator;
2. One (1) RIGOL DS1104Z Plus four-channel digital oscilloscope;
3. One (1) PC running MATLAB™ on Microsoft Windows 10;
4. One (1) aluminum acoustic energy harvesting disc;
5. One (1) 35 mm diameter center piezoelectric actuator; and

6. Nine (9) 5 mm diameter piezoelectric sensors.

Both the function/arbitrary waveform generator and digital oscilloscope were connected to the PC to for automated signal control and data acquisition. The function/arbitrary waveform generator was connected to the central piezoelectric actuator for applying desired frequencies to the AEH disc, and three channels of the digital oscilloscope were connected to three of the piezoelectric sensors at one time. The testing suite was performed three times, each time cycling through the next three sensors until data from all nine sensors were captured. One channel of the digital oscilloscope was always connected directly to the function/arbitrary waveform generator to serve as a reference input signal for comparing the measured signals received on the other three channels.

Table 7 lists the mounting positions of the nine piezoelectric sensors mounted on the underside of the AEH disc.

Table 7

Piezoelectric Sensor Array — Linear Positioning

Sensor	**1**	**2**	**3**	**4**	**5**	**6**	**7**	**8**	**9**
Distance From Center (mm)	21	42	63	84	105	126	147	168	189

Figure 24 illustrates the detailed layout and connections for the array of nine 5 mm piezoelectric sensors attached to the underside of the AEH disc.

Figure 24

Physical AEH - Piezoelectric Sensor Detail

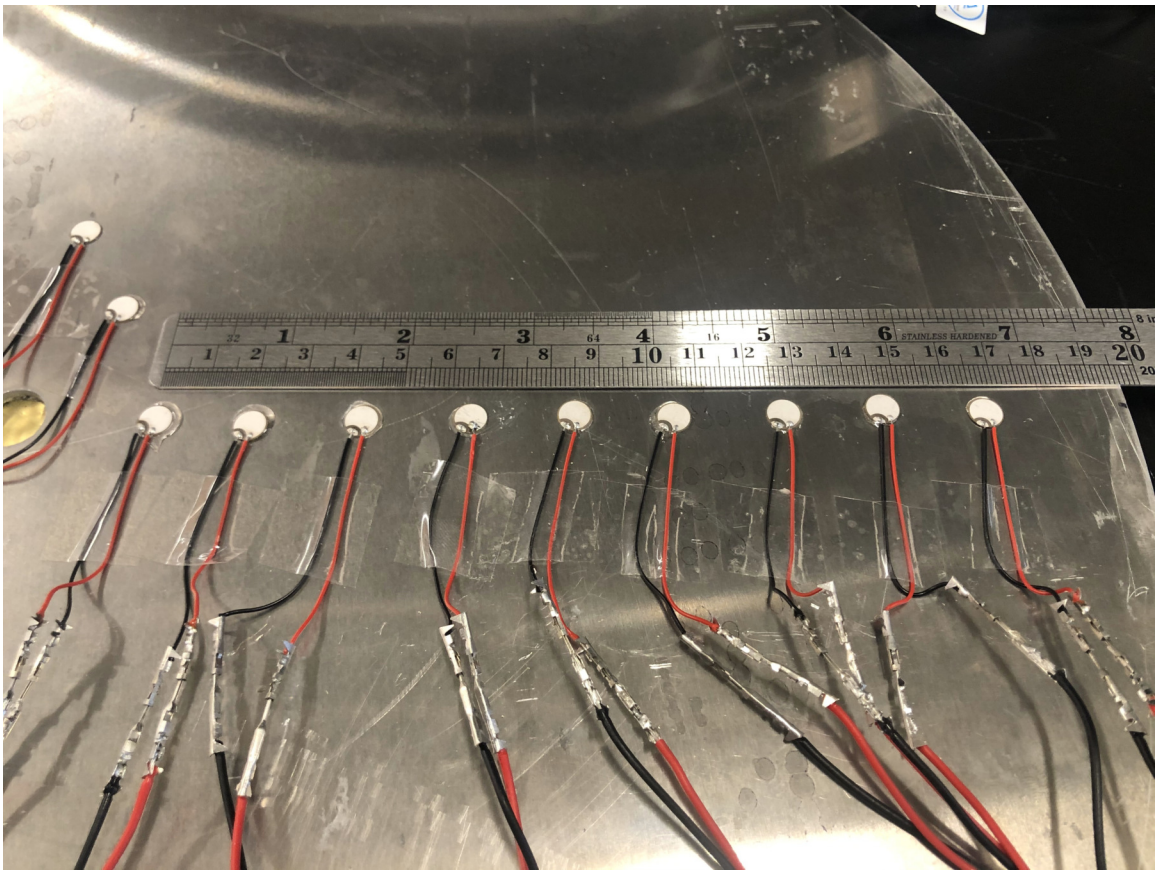

Note. The ruler is not part of the acoustic energy harvester disc. It is intended to illustrate the spacing distance between piezoelectric sensors mounted along the acoustic energy harvester disc.

5.5.1 Electrical Wiring

Each of the piezoelectric actuators and sensors used in the AEH prototype were connected to the function/arbitrary waveform generator and/or digital oscilloscope using two wires: one positive lead and one negative lead. These wires were cut into segments roughly 100 cm in length from a spool of 32 AWG stranded wire. Electronics wiring connectors were soldered onto the wires and piezoelectric devices to facilitate connection and reconfiguration of the testing apparatus, but this step was an optional convenience. A female electronics wiring connector was soldered onto each lead of each piezoelectric

device, and a male electronics wiring connector was soldered onto one end of each of the cut wire segments. The bare stranded wire ends of the wire segments were then twisted and connected to the function/arbitrary waveform generator and/or digital oscilloscope using standard BNC to probe clamp cables.

Aluminum is a highly electrically conductive material, so precautions were taken to ensure that any exposed wiring was not touching the aluminum AEH disc. Any inadvertent contact between the exposed wiring and aluminum AEH disc would have resulted in undesirable signal reduction. The wiring used was stiff enough to remain in place after being bent slightly, so the wires were bent in a way where the exposed metal components were suspended away from the surface of the aluminum AEH disc. This also had the benefit of reducing the wiring's overall contact surface area with the AEH disc since vibrations may be dampened by direct contact between the AEH disc and other materials. However, a permanent installation would have benefited from an insulated coating around the exposed wiring connectors and any other conductive materials within the wiring.

5.5.2 Attachment Methods

Since the measured results directly influenced by the vibrations that travel from the piezoelectric actuator through the aluminum AEH disc and into each piezoelectric sensor, it was critical to achieve direct and secure contact between the piezoelectric devices and the surface of the AEH disc. Multiple options were explored for securing the piezoelectric devices to the AEH disc:

1. Simply placing each piezoelectric device on the AEH disc using natural gravity;
2. Placing a weighted object on top of each piezoelectric device;
3. Clamping each piezoelectric device to the AEH disc; and
4. Attaching each piezoelectric device to the AEH using adhesives such as

(a) Common cyanoacrylate super glue;

(b) Conventional setting (24-48 hour) epoxy resin; and

(c) Quick-setting (5 minute) epoxy resin.

The less permanent options such as relying on gravity were unfortunately less effective than the permanent options such as epoxy adhesive. Placing a piezoelectric device on top of the AEH disc without any additional downforce or adhesive force was ineffective due to uneven contact between the piezoelectric device and AEH disc. While this was significantly influenced by the stiffness of the wiring leads attached to each piezoelectric device causing the devices to lift off of the surface of the AEH disc, straightening the wiring leads was unsuccessful at resolving this issue.

Conversely, induced downforce options such as using weighted objects or clamps were quite effective at ensuring direct and even contact between each piezoelectric device and the AEH disc. However, these options were largely unsuitable for this application since they acted as acoustic dampening materials, adversely affecting the frequency response received by each sensor. If this reduced frequency response were linear and consistent, then it could have been easily compensated for in the end results. However, the signal amplitude was reduced in an inconsistent and somewhat unpredictable fashion. Furthermore, the piezoelectric devices are only capable of withstanding a limited amount of applied pressure. Several piezoelectric sensors and actuators were damaged while attempting to determine the their ideal applied downforce.

With this in mind, adhesives appeared to be the clear choice for attaching the piezoelectric devices to the AEH disc. However, it was not entirely obvious at first which type of adhesive would work best in this application. Any material impeding direct contact between the piezoelectric devices and the AEH disc would have an adverse effect on the signals transmitted through the AEH disc. As such, the goal was to find an adhesive that could maintain a secure hold with the smallest material thickness possible. Additionally,

short curing times were best to avoid any possible drifting of the piezoelectric devices across the AEH disc during the setting process.

Cyanoacrylate super glue was initially selected due to its extremely short curing time ($<$ 5 minutes) and claimed compatibility between the brass material used in the piezoelectric devices and the aluminum material used in the AEH disc. However, this adhesive achieved a less secure hold than expected. Additionally, the low viscosity of this adhesive rendered it somewhat difficult to apply in a thin, even coating on the surface of each piezoelectric device.

Epoxy resin-based adhesive was the next most preferred attachment option. Such adhesives rely on mixing equal parts of epoxy resin and a hardening compound to result in a secure and durable hold. Epoxy resin-based adhesives tend to have a higher viscosity compared to other adhesives like cyanoacrylate super glue, and this facilitates the adhesive application process. However, some epoxy resin-based adhesives are somewhat slow to set, often taking up to 48 hours to completely cure [29]. While a slower setting epoxy adhesive resulted in a strong and secure attachment of the piezoelectric devices to the AEH disc, some of the piezoelectric devices drifted out of place over the long curing time due to some imperfection in the table's levelness. To avoid this issue, J-B Weld ClearWeld Quick-Setting Epoxy was ultimately selected due to its secure attachment and fast 5-minute setting time. These properties allowed the piezoelectric devices to have a thin and even layer of adhesive applied to them for a durable and secure attachment to the AEH disc.

5.6 Boundary Conditions

Each of the boundary conditions applied to the 2D axisymmetric AEH disc model in COMSOL Multiphysics® are also applicable to the physical prototype. As previously referenced in subsection 4.1.4, the AEH disc had the top surface assigned as a free boundary, the bottom surface as a rigid surface boundary, and the outer perimeter surface as a low-reflecting boundary. However, these are ideal boundary conditions. Applying ideal

boundary conditions to a physical prototype posed some challenges due to the differences between an ideal simulation and reality.

5.6.1 Physical Orientation

The three boundary conditions applied to the COMSOL Multiphysics® AEH disc model are somewhat dependent upon the physical orientation of the AEH disc. For example, the free surface and rigid surface boundary conditions are dependent upon which way the disc oriented in 3D space. If the disc is positioned on a flat surface with the grooves facing upwards, then the AEH surface featuring the groove openings is treated as top the free-space boundary condition. Conversely, positioning the grooves facing downwards on a flat surface requires treating the AEH face opposite of the groove openings as the top free-space boundary. The following physical orientations were evaluated during the physical prototype testing process:

1. AEH disc on a flat table under natural gravitational force with
    (a) Groove openings facing upwards; and
    (b) Groove openings facing downwards;
2. AEH disc clamped along its edges to a flat table with
    (a) Groove openings facing upwards; and
    (b) Groove openings facing downwards; and
3. AEH disc clamped vertically in one location near its outer edge to a vertical support.

Despite expectations, placing the AEH disc on a flat table under its own natural gravitational force proved to be the most effective overall physical orientation. No significant difference was found regarding having the groove openings facing towards or away from the table. As for the forced pressure physical orientation options, determining the

optimal clamping force was difficult. The results obtained during testing in these physical orientations indicated that even light amounts of clamping pressure significantly reduced the amplitude of signals received at sensors along the AEH disc. Such behavior was likely caused by the relatively high mass and large physical size of the clamp placed in direct contact with the AEH disc surface. The clamp appeared to be mimicking the behavior of an acoustic black hole [19] such that the acoustic waves seemed to be trapped within the clamp structure instead of freely propagating through the AEH disc structure. This effect was consistent even when the AEH disc was clamped to a fixed vertical surface using only one small clamp placed near the AEH disc's outer perimeter.

5.6.2 Free Surface Boundary Condition

Of the three ideal boundary conditions, the free boundary on one of the AEH disc's surfaces was perhaps the most straightforward to replicate in the physical prototype. This boundary condition is easily replicated by not having any solid objects touching the relevant surface of the AEH disc. In the AEH prototype, the only solid objects touching the free-space surface were the piezoelectric devices mounted on the face of the AEH disc subjected to the free surface boundary condition.

5.6.3 Rigid Surface Boundary Condition

Maintaining AEH structural rigidity is critical to ensuring adequate transmission of acoustic waves throughout the AEH. Inadequate AEH structural rigidity increases the likelihood of the AEH strucutre resonating with the free-space air, thereby leading to a reduction in the acoustic energy captured by the AEH [13]. This resonance effectively transforms the AEH structure into an acoustic reflector instead of an acoustic gatherer as a greater portion of the input acoustic waves are transmitted to the free-space air instead of through the AEH structure.

Furthermore, maintaining a rigid surface boundary condition for one of the AEH

disc's surfaces was explored in an attempt to minimize any acoustic vibrations being reflected back through the air. Rigid surfaces offer a higher acoustic transmission than air due to their higher density. By offering direct contact between the AEH disc and a rigid surface boundary, any acoustic vibrations escaping the AEH structure would tend to travel through this rigid surface instead of though the air. This results in fewer internal reflections within the AEH structure as well as potentially higher acoustic energy transmission efficiencies along the solid ungrooved surface of the AEH disc. A flat table emulated this boundary condition for the physical AEH prototype.

5.6.4 Low-Reflecting Surface Boundary Condition

A low-reflecting surface boundary condition was maintained for the outer perimeter surface of the AEH disc. While this surface is only 1/8 in. (3.175 mm) thick, it has the potential to play a significant role in the amount of internal reflections experienced by the AEH disc. As acoustic waves propagate from the center towards the outer perimeter of the AEH disc, they travel though the ungrooved portion of the AEH disc as well as through the air gaps formed by the grooves in the AEH structure. Acoustic waves reaching the outer perimeter of the AEH disc have the potential to continue traveling in the same direction, thereby exiting the AEH disc and entering the surrounding air. However, most acoustic waves reaching the outer perimeter of the AEH disc instead return along the same path that they already traversed. These internal reflections are caused by the fact that acoustic waves tend to propagate through the densest material. Such internal reflections increase signal analysis difficulty since any given piezoelectric sensor may read both the primary incident wave as well as any reflected waves traveling past them. Various reflection dampening materials were evaluated for attachment to the outer perimeter of the AEH disc in an attempt to minimize any internal reflections.

5.6.5 Reflection Dampening Materials

Three primary reflection dampening materials were evaluated along the AEH disc perimeter during the AEH disc prototype testing process:

1. High-density polyurethane packaging foam;
2. Play-Doh Classic brand starch-based modeling compound; and
3. PVC-based polymer modeling clay.

Each reflection dampening material candidate was selected for its ease of application along the AEH disc perimeter, acoustic insulation potential, and electrical insulation properties. Polyurethane packaging foam appeared to produce detrimental results to the AEH disc prototype. Acoustic waves received at most of the piezoelectric sensors were lower in amplitude than without the polyurethane foam, and there was less separation defined between the incident wave and any internally reflected waves.

Play-Doh Classic initially appeared to be a promising alternative due to its high density, pliability, and ease of application. While it remained moist, this modeling compound displayed a mild reflection dampening effect. However, this modeling compound quickly hardened as it desiccated in normal room temperature and humidity conditions. This resulted in separation between the modeling compound and the aluminum AEH disc, thereby diminishing any reflection dampening performance. An unintended consequence of using Play-Doh Classic was that some parts of the modeling compound would flake off after drying, and this resulted in uneven surface contact between the table, modeling compound, and AEH disc.

PVC-based polymer modeling clay also initially appeared to be an even more promising alternative to starch-based modeling compound since polymer clay does not desiccate under normal room conditions. This allows the clay to maintain its pliability and reflection

dampening effect. However, this polymer modeling clay demonstrated a minimal reflection dampening effect. Furthermore, the adhesive nature of this modeling clay made it somewhat difficult to reposition or remove the AEH disc from the table. Ultimately, final AEH disc prototype performance testing was conducted without any perimeter reflection dampening materials due to their insignificant improvement regarding internal reflections and their corresponding disadvantages outweighing any observed benefits.

Chapter 6

Data Acquisition, Processing, and Results

6.1 DAQ Configuration

Data acquisition (DAQ) was of critical importance for verifying the performance of the physical AEH disc prototype against the simulated results. Signals were applied to the AEH disc prototype using an automated command structure to repeat a defined evaluation cycle with a progressive increase in input frequencies ranging from 100 kHz to 220 kHz. This evaluation cycle was designed to repeat an identical set of induced signals to complete capture the resulting incident waves trapped across the entire AEH disc prototype structure.

These induced signals were pulse waves with sinusoidal behavior. However, sinusoidal signals are subject to aliasing where the signals cannot be adequately reconstructed without a sufficient data sampling rate. The Nyquist sampling rate refers to the safe minimum signal sampling rate to ensure adequate reconstruction of sinusoidal signals, and this rate is equal to twice the highest frequency observed in the sample data [30]. This study's highest input signal frequency was 220 kHz, and the measured signals should not exceed this frequency. As such, the Nyquist sampling rate for this scenario was 440 kHz.

Unfortunately, PC-connected DAQ systems are limited by an overall signal sampling frequency that is shared between all of the simultaneously active signal input channels. This means that each active sampling channel may only use a fraction of the DAQ's overall sampling rate. If a given DAQ has an overall sampling rate of 1 MHz, then sampling four channels simultaneously limits each input channel to a sampling frequency of one fourth of the 1 MHz overall DAQ sampling rate, 250 kHz. This presents a potential issue when selecting DAQ solutions for use with high-frequency sampling applications.

While the minimum DAQ configuration would consist of one input channel per evaluation cycle, using multiple input channels per evaluation cycle is more convenient and time-efficient. This study intended to evaluate the AEH disc prototype's rainbow trap-

ping performance at various points along the disc's structure, so using an array of multiple sensors was the obvious choice. It was not quite as obvious exactly how many sensors should be used, nor was it obvious how many of these sensors could be simultaneously evaluated during any given evaluation cycle. An array of nine identical sensors linearly spaced along the AEH disc prototype was implemented as a reasonable compromise between sensor placement density and testing time requirements.

To reduce the required number of evaluation cycles and associated testing time, simultaneously sampling as many input channels as possible is preferred. However, this is limited by a given DAQ's overall shared sampling rate, the number of simultaneous sampling channels in question, and the aforementioned Nyquist sampling rate of 440 kHz for this study. An ideal configuration would include simultaneously sampling one channel for the induced waves as well as the nine channels for the received incident waves. As such, an ideal DAQ would need to provide an overall shared sampling rate of 440 kHz multiplied by the ten simultaneous sampled channels, resulting in a minimum global sampling rate of 4.4 MHz. Unfortunately, sourcing an affordable, ten-channel, PC-connected DAQ with a minimum global sampling rate of 4.4 MHz proved to be quite difficult. While potentially connecting multiple DAQs to the experiment control PC may have been possible, there were concerns regarding the complexity and reliability of such a configuration.

A RIGOL DS1104Z Plus four-channel digital oscilloscope was selected as a reasonable compromise between its relative affordability, maximum simultaneous data channel capacity of four channels, and global sampling rate of 1 GHz. This results in a minimum sampling capacity of 250 MHz per channel, greatly outperforming the required Nyquist sampling rate for this scenario. Offering four simultaneous data channels, this oscilloscope helped minimize the required number of evaluation cycles to three evaluation cycles per configuration. During any given evaluation cycle, the oscilloscope would sample the signals being applied to the AEH disc prototype on one input channel, and it would also sample three of the nine received incident signal sensors using the remaining channel capacity.

This process was repeated twice to collect data from all nine incident wave sensors.

6.2 System Configuration Overview

The acoustic energy harvesting performance was evaluated by subjecting the energy harvester disc to pulse signals ranging in frequency from 100 kHz to 220 kHz and measuring the resulting frequency response at various locations across the disc structure. The center 35mm PZT piezoelectric actuator disc was connected to a RIGOL DG4162 function/arbitrary waveform generator. An array of nine 5 mm diameter PZT piezoelectric sensor discs was connected to a RIGOL DS1104Z Plus four-channel digital oscilloscope. Both the function/arbitrary waveform generator and the digital oscilloscope were connected to a standard PC via the USB interface. The signal generation and measurement processes were automated using a MATLAB™ command and control script that simultaneously controlled both instruments.

6.3 Signal Generation

6.3.1 Generated Signal Type Selection

This study intended to evaluate the rainbow trapping performance of acoustic waves traveling through the designed AEH prototype disc structure. Selecting an appropriate type of induced signal was of critical importance since it would directly influence the incident signals received after the waves propagated throughout the AEH prototype disc's structure. While sinusoidal, square, triangle, and sawtooth waves are all commonly available for generation with modern function generators, most naturally occurring acoustic waves are sinusoidal. Since the AEH prototype design intended to capture energy from such sources of acoustic waves, sinusoidal induced signals were most appropriate.

However, continuous sinusoidal input waves repeat their pattern without interruption. Any AEH structure will experience some level of internal reflection, but an AEH's

rainbow trapping performance is measured solely using its intended received incident signals. Internally reflected signals obfuscate the intended incident signals, and the incident signals must then be isolated from any internally reflected signals for further analysis. Unfortunately, the repeating pattern of continuous sinusoidal input waves presents significant challenges when attempting to separate the incident waves of interest from any internally reflected waves present within the received signals. This can be alleviated with the use of pulse signals for the AEH disc's induced input waves.

Any of the aforementioned wave types can be easily transformed into their corresponding burst signals by simply not continuously repeating the wave. Using a sinusoidal burst input wave with a delay between induced burst signal groups allows for the AEH disc structure to return to its default state as any internally reflected waves have sufficient time to propagate throughout the AEH disc structure. Intended incident waves generally travel directly from the signal inducer to the signal receiving sensor, but internally reflected waves first travel this same path, then travel back to the receiving sensors. Since intended incident waves are expected to reach any given sensor before any internally reflected waves, isolating the intended incident waves is as simple as selecting the first group of received signals within the specified signal group delay period. This provides superior signal measurement performance compared to the discussed alternatives.

6.3.2 Pulse Signal Generation

Acoustic waves are generated using a RIGOL DG4162 function/arbitrary waveform generator in conjunction with a MATLAB™ command and control script. Burst waveforms are specifically generated using a dedicated function that is called by the main signal command script. This function, `sig_gaussian_pulse_int_14bit.m`, creates a pulse with a Gaussian envelope by importing the desired signal frequency components, sampling frequency, signal length, pulse center, and pulse width as variables from the main signal generation script. The function uses these variables to create an array of signal am-

plitude values over a span of time, and it then passes those signal amplitude and timestamp values back to the main signal command script for transmission to the physical waveform generator. Appendix B contains the entire burst signal generation code.

6.4 Signal Acquisition

One master command and control script simultaneously handled generating induced signals for application by the function/arbitrary waveform generator to the AEH disc prototype's center piezoelectric actuator as well as collecting measured signals received on three oscilloscope channels from the piezoelectric sensors and on one channel from the function/arbitrary waveform generator. Oscilloscope channel 1 was connected to the function/arbitrary waveform generator, and this channel was used to calibrate the sensor signals received on oscilloscope channels 2-4 against the signals that were physically applied to the AEH disc prototype.

This master command and control script generated induced signals, applied those signals to the AEH disc prototype using the function/arbitrary waveform generator, and collected signals received by the oscilloscope. Since only three channels were available for connection to the piezoelectric sensors measuring the incident waves across the AEH disc prototype, the command and control routine was performed three times for each evaluation cycle to collect data from all nine incident wave sensors. Appendix C contains the entire signal acquisition code.

6.4.1 Function/Arbitrary Waveform Generator

The master command and control script uses the aforementioned pulse signal generation script to generate consistent sinusoidal pulse signals ranging from 100 kHz to 220 kHz in 2 kHz increments. The command and control script interfaces with the function/arbitrary waveform generator as a VISA-USB object, and this allows the script to automatically apply the generated signals to the AEH disc prototype's center piezoelectric actua-

tor. This method of using a VISA-USB object essentially sends a stream of serial data to the function/arbitrary waveform generator with the desired wave characteristics, and the function/arbitrary waveform generator reliably generates physical waves with the specified characteristics.

Successfully controlling the function/arbitrary waveform generator required tuning several parameters including:

1. Output buffer size in bytes (`OutputBufferSize`);
2. Signal output voltage in V_{pp} (`voltage`);
3. Output sampling rate in Hz (`fs`);
4. Number of cycles per sigma of the Gaussian pulse (`cyc_per_sigma`); and
5. Duty cycle (`duty_cycle`).

To begin, the output buffer size limits the size and type of waveforms that can be sent to the function/arbitrary waveform generator. Larger or more complex waveforms require a larger corresponding buffer size to contain the necessary data for generating the waveform. While the default value is 512 bytes (B), attempting to use such a small buffer size risks encountering communication errors for many complex waveform types. Other than excessive memory consumption on the controlling PC, there appears to be little downside to using an oversized output buffer. However, this is an insignificant problem given that modern PCs often contain much more system memory than required for this operation. As such, an output buffer size of 512 B * 1024 = 512 KiB (524.288 kB) was chosen to prevent any potential errors related to output buffer overflow.

Next, the signal output voltage determines what voltage is physically applied to the piezoelectric actuator. This output voltage is directly proportionate to the amplitude of the waves produced by the piezoelectric actuator. While using a smaller signal output voltage can increase the difficulty of measuring the incident waves due to systematically lower

signal amplitudes, specifying an excessive voltage can damage a piezoelectric actuator. As such, a signal output voltage of 25 V_{pp} was selected to match the piezoelectric actuator's rated maximum safe voltage.

Moreover, the output sampling rate specifies the frequency that the function/arbitrary waveform generator uses to generate the specified waveforms. This differs from the actual frequencies of the generated waveforms. Instead, the output sampling rate is a measure of the function/arbitrary waveform generator's swiftness to change between different waveforms. The RIGOL DG4162 function/arbitrary waveform generator used in this study offers a maximum output sampling rate of 500 MHz, so the output sampling rate specified by the command and control script is ultimately limited by this value. However, this value must be harmonized with the oscilloscope's maximum per-channel sampling rate. When simultaneously measuring signals from four channels, the RIGOL DS1104Z Plus four-channel digital oscilloscope used in this study offers a maximum sampling rate of 250 MHZ. As such, the command and control script specified a 250 MHz sampling rate to capture maximum possible resolution in the oscilloscope's received signals.

Furthermore, the number of cycles per sigma of the Gaussian pulse refers to the number of times that the function/arbitrary waveform generator inverts signal polarity within a generated pulse signal period. This value significantly influences the ease of measuring the resulting pulse signals. The absolute peak of a pulse signal can be configured to occur in the center of the signal with the other local signal peaks symmetrically surrounding the center peak. This facilitates pattern matching between the generated pulse signals and the measured signals. The number of cycles per sigma value determines the number of peaks that are expected in the pulse signal. This study explored different values for this variable and settled on a value of 10 cycles per sigma.

Lastly, the duty cycle specifies the portion of an signal on/off cycle that the signal is actively being sent to the function/arbitrary waveform generator. The duty cycle is represented in a decimal range where 0 is equivalent to the signal being inactive for the entire

on/off cycle and where 1 is equivalent to the signal being active for the entire on/off cycle. This is a technical specification that plays a critical role in coordinating compatible technical specifications between the function/arbitrary waveform generator and oscilloscope.

In conjunction with the output sampling rate supported by the function/arbitrary waveform generator, this duty cycle value influences the swiftness and separation of the generated signals. If the duty cycle is too high, this results in less spacing between the pulse signals. Increased pulse crowding increases the difficulty of distinguishing between a primary pulse measurement and a secondary or reflected signal measurement. Effectively separating primary signals from reflected signals was important for evaluating the acoustic wave rainbow trapping performance of the AEH structure. This study explored several duty cycle options, but a duty cycle of 0.01 resulted in the most reliable results overall.

6.4.2 Oscilloscope Signals

The next step in the command and control script is reading the signals received from the oscilloscope. The oscilloscope simultaneously measures four data channels with the first channel being connected directly to the function/arbitrary waveform generator and the other three channels being connected to piezoelectric sensors at defined spacing intervals along the surface of the AEH. Successfully controlling the oscilloscope required tuning multiple parameters including:

1. Input buffer size in bytes (`InputBufferSize`);
2. Output buffer size in bytes (`OutputBufferSize`);
3. An initialization pause in seconds; and
4. A cycle separation pause in seconds.

The input and output buffer sizes refer to the amount of data that is locally stored, or buffered, within the digital oscilloscope. Larger buffers tend to offer greater protection against momentary interruptions in data flow between the controlling computer and

the oscilloscope, but the maximum buffer size is limited by both of these components. Conversely, an insufficient buffer size may result in data loss in the event of data stream interruptions. Such data stream interruptions may be caused by a variety of unexpected issues such as controlling computer CPU delay, memory errors, or USB-related transmission errors. As such, this study selected input and output buffer sizes of 10,000 B (10 kB) to ensure a reasonable balance between the buffered data and any possible PC and oscilloscope hardware limitations.

While supplying the AEH structure with pulse signals from the function/arbitrary waveform generator, the command and control script incorporates an initialization pause of five seconds before attempting to read the resulting signals using the oscilloscope. This delay ensures that the pulse signals stabilize within the AEH structure prior to reading. Without this delay, it is possible that the oscilloscope would receive truncated signals from the function/arbitrary waveform generator. The five-second initialization pause was selected for compatibility with the output sampling rate and duty cycle values used for the function/arbitrary waveform generator.

Similar to the initialization pause, the command and control script uses a cycle separation pause of three seconds. This cycle separation pause intends to allow any signals to fully dissipate within the AEH structure prior to beginning the next cycle of generating a pulse signal and measuring the incident waves from the AEH. Without such a pause, signal measurements between measurement cycles would overlap. Such overlap would render it difficult to distinguish one group of signals from the next. The three-second cycle separation pause ensures that cycles are adequately separated for later analysis and comparison against the generated pulse signals.

6.5 Signal Processing

After collecting raw amplitude data from the array of nine piezoelectric sensors, these data were processed into a plot illustrating the frequency response curves at various

physical locations along the AEH structure. Signal processing is of critical importance since it suppresses random noise that is present in all electronic devices while clarifying the AEH's acoustic rainbow trapping performance metrics. The signal processor emulates in software what would otherwise be achieved using signal conditioning devices while avoiding data distortion. Appendix D contains the entire signal processing code.

The first step in the signal processing procedure is to analyze the frequency data collected from the oscilloscope. Data are loaded in batches of three sensors at one time with the function/arbitrary waveform generator data for comparison. Then, the signal offsets are cleared so that all signals have a zero mean value. This step is performed to suppress any present electronic noise. Next, the signals are normalized to account for each subsequent sensor's increasing physical distance from the center of the AEH disc. This is accomplished by multiplying each sensor value by the sensor's radius from the center of the AEH disc. After this, the signal processor begins the frequency analysis procedure.

6.5.1 Frequency Analysis

The frequency analysis procedure begins with discarding all data that fall outside of the targeted frequency range of 100 kHz - 220 kHz. This step ensures that any attenuated waves received outside of the frequency input range do not contaminate the analyzed data. Next, a series of three nested loops perform several functions. The outermost loop performs the entire nested process for each batch of data collected from the oscilloscope (up to four channels per batch). The second loop performs all nested operations for each of the evaluated frequencies.

Within the innermost loop, a fast Fourier transform (FFT) routine is applied to the remaining data of interest. This loop cycles through a range of estimated sampling rates until it converges upon each dataset's actual sampling rate. It accomplishes this by first finding the index location where the peak amplitude is found within the FFT output, then minimizing the difference between the frequency found at this index location and the actual

frequency value that is currently being evaluated. Then, the innermost loop procedure uses the control data channel index to assign the determined sampling frequency and peak amplitude index values to each of the three captured sensor data streams corresponding with that specific control data channel.

Following the three-level nested loop, another loop cycles through the each of the evaluated frequencies to find the envelopes of the input signals. These signal envelopes and max signal index values are stored in separate arrays for later use.

After this loop, a two-level nested loop performs several operations. The outer loop performs all nested procedures for each data channel received from the oscilloscope while the inner loop cycles through each of the evaluated frequencies. This inner loop uses the calculated sampling rates for each frequency to determine the width of the window applied to the signals, then it finds the local peaks of the signals within the corresponding window. The loop then finds the index of the first peak following the peak index of the input signal, and it truncates the signal range extending beyond the calculated window. After this, the loop calculates the spectrum amplitude of the signals within the window, and it applies two FFT functions to find the FFT amplitude and FFT frequency values along with the spectrum phase angle. Lastly, this loop stores the FFT amplitude and phase values corresponding to the peak index values in separate arrays for later use.

6.5.2 Sampling Frequency Calibration

The next major processing step involves normalizing the amplitudes of the measured signals. This step begins with defining the frequency range of interest and the desired incremental stepping value of 30 kHz in this case. Then, three separate loops calculate the normalized FFT amplitudes for each group of three sensors. Next, a two-level nested loop performs several operations. The outer loop performs all nested procedures for each discrete analyzed frequency, and the inner loop performs all operations for each of the nine sensors. This loop first finds the index of the lower bound of the band, then it finds the

index of the upper bound of the band. Next, the FFT amplitudes are truncated to only retain values corresponding to the discrete frequencies of interest. After this, the loop assigns the final frequency response value corresponding to each sensor channel. Thereafter, the datasets are scrubbed of any zero-value placeholder values. They are then sorted to facilitate data review.

Finally, the signal processor displays a plot of the normalized frequency amplitudes across the evaluated frequency range. These results are displayed for each of the physical sensor locations attached to the AEH disc structure, and they illustrate the AEH's acoustic rainbow trapping performance for these frequencies across the AEH structure.

6.6 Results

The AEH prototype's acoustic wave rainbow trapping performance is primarily evaluated using the normalized amplitudes for each of the nine sensors across the frequency range of interest. When coupled with each sensor's corresponding radius value listed in Table 7, peaks in the normalized amplitude plot illustrate physical locations on the AEH prototype disc where acoustic waves of the corresponding frequency are most effectively trapped. Figure 25 illustrates the normalized AEH frequency response measurements for each sensor across the frequency range of interest.

Figure 25

Measured AEH Frequency Response Curves — Processed Results

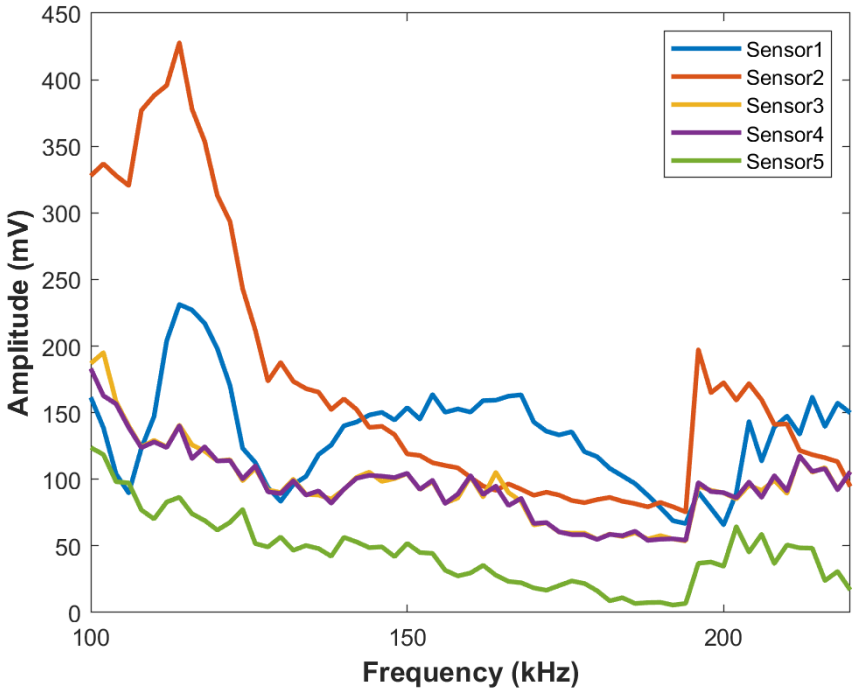

(a) *Sensors 1-5*

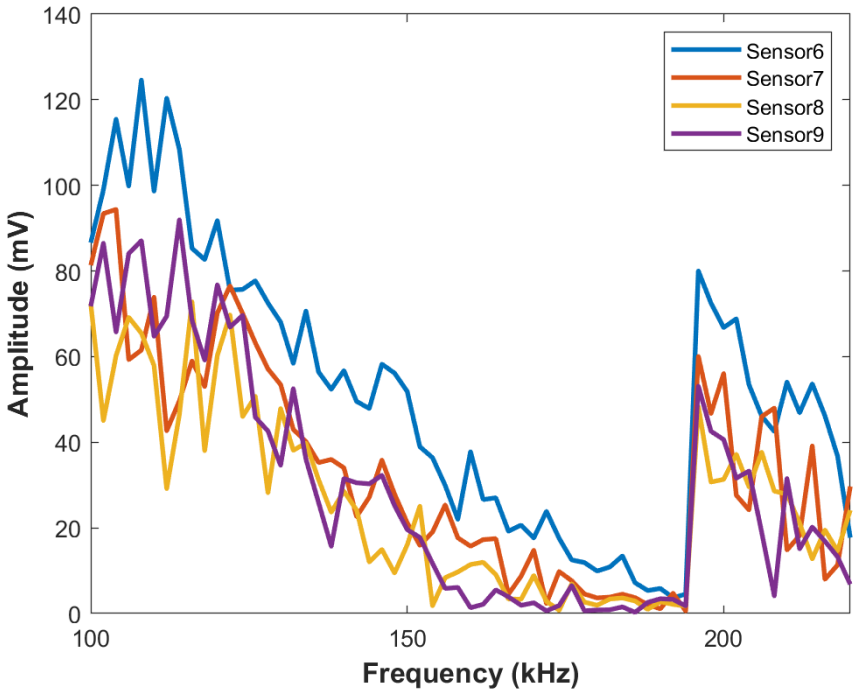

(b) *Sensors 6-9*

Acoustic waves of a given frequency within the evaluated frequency range are most effectively captured at the location of the sensor(s) where frequency response peaks are present. As can be seen in Figure 25, a general trend exists where frequency response peaks are present at higher frequencies for lower sensor numbers and at lower frequencies for higher sensor numbers. Since higher sensor numbers correspond with increasing physical distance from the center of the AEH prototype disc, this trend indicates that frequency and sensor radius are inversely proportional for this AEH design.

However, the normalized frequency response plot illustrates some exceptions to this trend for most of the sensors around 120 kHz - 130 kHz and 190 kHz - 200 kHz. In these two frequency ranges, most of the sensors appear to exhibit elevated acoustic wave trapping performance compared to the rest of the evaluated frequency range. Other sensors, such as sensor 5, exhibit multiple peaks of similar amplitude. This indicates that this particular location on the AEH disc are moderately adept at trapping acoustic waves of these corresponding frequencies. Multiple such peaks appearing for a given sensor can be evidence of internal reflections within the AEH disc structure redirecting secondary frequencies to the physical location on the AEH disc corresponding to the particular sensor.

Furthermore, some sensors such as sensor 8 exhibit relatively flat frequency response curves of somewhat low amplitude. This illustrates that the given sensor did not perform as well as its peers for trapping acoustic waves within the frequency range of interest. This could indicative of a physical connection fault with the piezoelectric sensor, or it could potentially indicate that the AEH disc structure at the corresponding location is not appropriately suited for high-efficiency trapping of acoustic waves within the frequency range of interest. This and other possibilities would present promising opportunities for future investigation and improvement.

Chapter 7

Conclusions and Future Work

This study sought to investigate the acoustic energy harvesting performance of various unit cell types and to design a 2D axisymmetric AEH using an array of unit cells with optimal acoustic wave rainbow trapping properties. This chapter is organized as follows:

1. Analysis of acoustic wave capture efficiency;
2. Evaluation of energy harvesting performance;
3. Discussion of future developments and improvements; and
4. Exploration of AEH technology's integrations and applications.

7.1 Acoustic Wave Capture Efficiency

Acoustic wave capture efficiency is evaluated using the normalized frequency response curves presented in the results section of this work. Localized peaks indicate greater capture of acoustic waves of the active frequency at the corresponding sensor location. Since the unit cell width increases with increasing distance from the center of the AEH disc, this AEH was designed to exhibit a predictable wave trapping pattern at any distance along the AEH disc.

As discussed in the results section, the overall frequency response trend observed in this study was consistent with expectations. However, some of the observed frequency response behaviors were somewhat unexpected. For example, nearly all of the sensors demonstrated significant responses in the 120 kHz - 130 kHz range. This implies that the entire AEH disc structure is well-suited to trapping acoustic waves within this narrow frequency range, but this result is somewhat disappointing since the study intended to provide greater precision and consistency in the predicted frequency response variations. Such a

result implies that the AEH design is not quite as optimized as expected since it is trapping certain frequencies across the entire AEH disc instead of localizing trapping to designated regions along the AEH disc.

Furthermore, the AEH design was expected to exhibit a very clear rainbow trapping pattern across the sensors. The pattern exhibited in the results is not quite as clear as expected. Instead of exhibiting a clear step-like pattern where the frequency response peaks occur at consistently-decreasing frequencies and amplitudes as sensor number increases, this pattern is somewhat obscured by unexpected inconsistencies. While the overall trend is evident, the transitions between individual sensor measurements are not quite as consistent as the trend predicted.

Lastly, some of the sensors experienced multiple peaks of similar magnitude across multiple frequencies. Rather than exhibiting the intended sharp delineation between frequencies trapped at various physical locations, the measured results illustrate that the physical AEH disc is somewhat less predictable compared to the ideal simulation model. This implies that the physical AEH disc is not achieving its peak potential acoustic wave rainbow trapping performance since some frequencies are not being trapped at their intended locations. Such results may have several potential causes including internal wave reflections, external interference, potential manufacturing errors, and other related problems. Fortunately, reasonable results were obtained with this study. However, these potential issues should be investigated in a future study to improve upon this AEH prototype design for use in a practical application.

7.2 Energy Harvesting Performance

The AEH's energy harvesting performance is a function of its acoustic wave capture efficiency and the efficiency of the specific piezoelectric acoustic transducers used to convert acoustic waves into electrical energy. Since a given type of piezoelectric acoustic transducer should maintain a fairly constant energy conversion efficiency factor, the

AEH's overall energy harvesting performance should be directly proportional to its acoustic wave capture efficiency for the frequencies its experiences within its intended environment. However, certain interference due to electrical short circuiting between the piezoelectric acoustic transducers and the surrounding environment or improper installation can negatively impact the useful electrical energy captured by the AEH. As such, it is crucial to critically consider an AEH's boundary conditions that it will experience within the intended operating environment.

This study did not directly measure the electrical current, voltage, and corresponding power output produced by each piezoelectric sensor attached to the AEH disc. Instead, it evaluated energy harvesting performance by measuring the frequency response curves for each of the sensor locations. While this is a reasonable approach for evaluating the AEH's acoustic wave rainbow trapping abilities, a future extension of this study could directly compare the electrical voltage and current outputs of each piezoelectric sensor against the power supplied to the center piezoelectric actuator to calculate an AEH system-wide specific energy harvesting efficiency value.

7.3 Future Investigations and Improvements

While reasonable results were obtained through this study, there are several improvement opportunities. These opportunities involve:

1. Expanding the range of frequencies of interest;
2. Minimizing internal reflections; and
3. Investigating the effects of physical scale.

7.3.1 Frequencies of Interest

Although this study explored the AEH's wave trapping performance in the range of 100 kHz to 220 kHz, an AEH's operational frequency range is ultimately determined

by the frequencies that are expected to be present in the AEH's intended environment as well as the AEH's physical space constraints within said environment. Hypothetically, an AEH can be designed to capture the entire possible range of acoustic frequencies, but this quickly becomes impractical since the AEH's physical size increases as the intended acoustic frequency capture range expands. Growth in a given AEH's physical size leads to corresponding increases in material use and cost. As such, it is important to match an AEH design to optimize acoustic wave capture efficiency in its intended application environment. Exploring acoustic frequencies outside of the 100 kHz - 220 kHz range would allow for AEH designs that can accommodate differing physical packaging restrictions.

7.3.2 Internal Reflection Minimization

An AEH's primary objective is to capture acoustic waves as effectively as possible. However, evaluating an AEH's wave capture effectiveness depends heavily upon accurately measuring the frequency response for incident waves that are trapped at specific locations within the AEH structure. Internal reflections within the AEH structure hinder the AEH's performance since waves lose energy as they propagate past the intended capture point. These internally reflected waves reach the outer edge of the AEH structure and return towards the center, but reflected waves possess less energy compared to incident waves that are captured at the intended location. As such, minimizing internal reflections is crucial to maximizing an AEH's acoustic wave rainbow trapping performance.

Boundary conditions play a significant role in influencing a given AEH's tendency to experience internal reflections. These boundary conditions are largely a function of the material interface between the AEH structure and its surrounding environment, but they can also be a function of the AEH structure material itself. Differing configurations and orientations of the AEH structure in physical space can have a significant impact upon the measured results. For example, either side of the AEH disc can be placed on a flat surface, it can be insulated at the edges using an acoustic dampening material such as clay or high

density foam, or the AEH disc can be suspended in air with minimal direct contact with any solid objects.

Since acoustic waves tend to propagate through the most permissive material, solid, rigid objects such as the AEH disc structure itself provide the best opportunity for wave propagation. This leads to an increased chance of internal reflections if the material in contact with the AEH structure is less permissive to acoustic wave propagation than the AEH disc material. However, dense and flexible materials such as clay or high-density foam tend to readily absorb acoustic waves. These materials could reduce the occurrence of internal reflections within the AEH structure. With this in mind, the use of dampening materials to alter an AEH's boundary conditions requires additional investigation.

7.3.3 Physical Scale

The physical size of an AEH is directly related to the acoustic wave frequency range that it is best suited to capture. This study used an AEH disc 451.7 mm in diameter and 3.175 mm in thickness because this scale facilitated signal measurement across the 100 kHz - 220 kHz frequency range of interest. However, many potential applications of AEH technology may not offer physical compatibility with this size of AEH device. Some applications may require much smaller AEH devices, and others may be better suited to even larger AEH devices. A smaller AEH device can be designed to optimize capture efficiency either for a narrow range of lower frequencies or a wider range of higher frequencies since the AEH's unit cell physical feature size is inversely proportional to the acoustic frequency of interest. Conversely, larger AEH devices may benefit from a wider range of captured acoustic frequencies or from the ability to capture lower frequencies of acoustic waves.

7.4 Integrations and Applications

7.4.1 Structural Health Monitoring and Longevity

A novel application of AEH technology is in structural health and longevity monitors. As vehicle and building structure designs become increasingly complex, additional opportunities for structural failure are introduced into a given structural system. Such failures must be preemptively resolved prior to developing into irreversible catastrophic failures. Periodic inspection programs are frequently used to monitor the overall health of a structural system, but the complexity of modern structural designs increases the difficulty for manual completion of comprehensive inspections. As such, many structural designs now incorporate automated structural health monitoring devices to continuously track a structure's health and issue alerts prior to structural failure [31].

Aircraft and spacecraft are two prominent applications of automated structural health monitoring systems. Aerospace applications are generally mission-critical due to the sorts of payloads carried by such vehicles as well as the potential for damage to the vehicle, its occupants, and others in the surrounding environment in the event of a catastrophic structural failure. Such vehicle structures are subjected to both strain from vibration as well as thermal fatigue from thermal gradients. When AEH devices measuring vibration-induced strain are coupled with thermoelectric generators measuring thermally-induced fatigue, these can serve as a comprehensive structural monitoring system for an aerospace vehicle [32].

7.4.2 Passive Energy Collection

One particularly useful application of AEH technology is the passive collection of energy. While countless devices can make use of electrical energy, the vast majority of them are powered by active electricity generation methods such as traditional power plants. Active electricity generation methods typically require continuous maintenance as

well as a fuel source, and these present additional complexities for any devices that may not be suited for tethering to the power grid. Passive acoustic energy collection allows devices and their energy collectors to be located near each other while transforming an otherwise unused form of energy into useful electrical energy. This is particularly useful in situations where predictably and reliably high intensities of acoustic waves are experienced. Larger vehicles such as locomotives and trucks are two common predictable sources of high-intensity sound.

Figure 26 illustrates an example of using AEH structures in railway noise barriers to both capture acoustic energy while reducing acoustic disturbance to the surrounding area.

Figure 26

AEH System — Railway Noise Barrier [33]

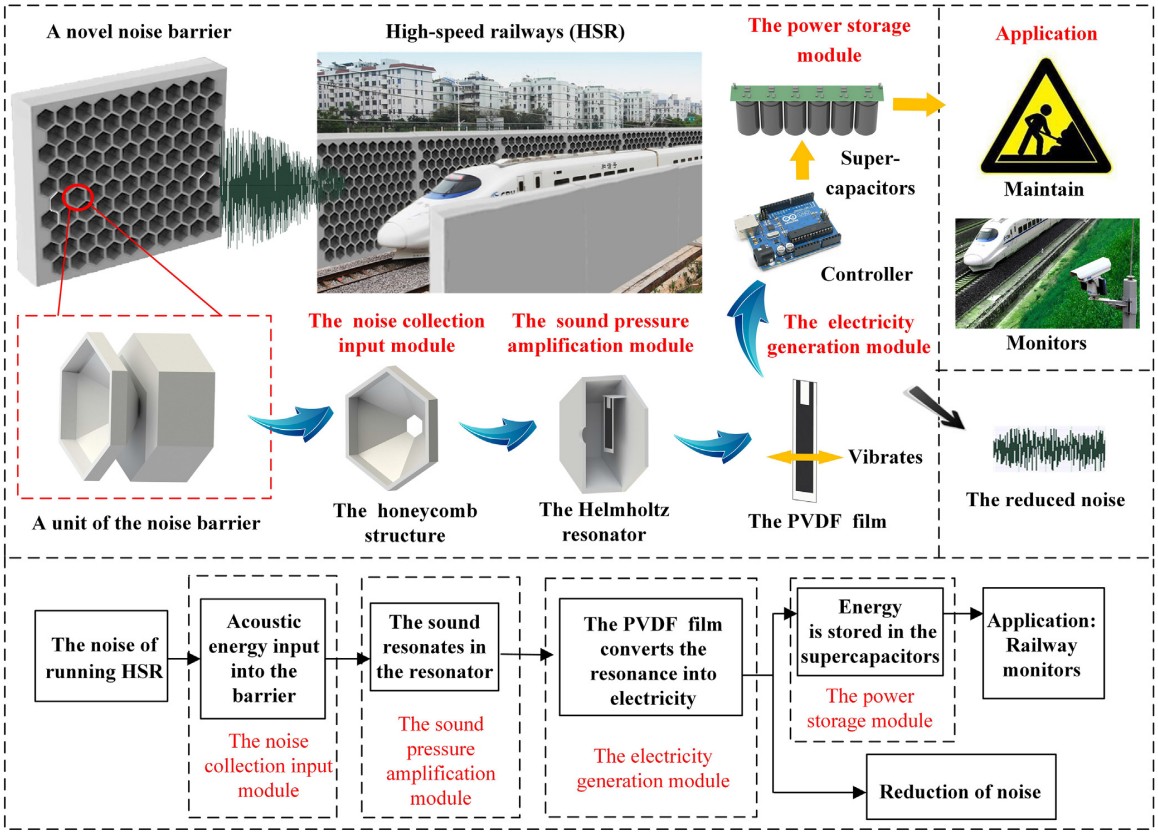

Noise complaints are a common occurrence from residents neighboring high speed railways. Since the noise produced by a vehicle is typically proportional to its speed, high speed railways are particularly notorious for causing acoustic disturbances. Such railways often have purpose-built acoustic barriers to reduce disturbance to the surrounding areas, but these are rarely used for any purpose other than isolating the railway from the environment. However, AEH structures integrated into the acoustic noise barriers could transform what would otherwise be a nuisance into a usable and dependable source of electrical energy. This electrical energy could be used to power devices such as railroad signals, maintenance probes, or security equipment without requiring dedicated hardwiring to the electrical grid. Furthermore, such acoustic noise barriers incorporating AEH structures can offer enhanced acoustic insulation compared to conventional acoustic noise barriers.

7.4.3 Acoustically Activated Electronics

With the rapid increase in the number of active electronics operating continuously in homes, commercial buildings, industrial production centers, vehicles, and transportation corridors, energy supply must increase accordingly to meet the demand of these devices. One common example is a voice-activated smart home speaker where a home may contain several such devices in various rooms. However, supplying electrical energy to such devices can often be difficult or inconvenient if such devices are not located near existing power sources. Harvesting acoustic energy from the device's environment would allow such devices to be located completely independently from traditional energy points such as a hardwired power outlet or a wireless charging pad. In the case of a smart home speaker, acoustic energy harvesting would be extraordinarily convenient since the devices explicitly intend for the user to speak to the device. The user's voice could potentially provide enough energy for the device to perform simple listening tasks.

Various acoustic sensors are used in a multitude of commercial, industrial, and transportation applications, and they all require connections to traditional energy sources.

While some of these devices are connected to more localized energy sources such as micro wind turbines or portable solar panels, these localized energy sources are not always practical with regards to cost or physical size for certain applications. This poses a great challenge for devices located in more remote areas such as railroad signals. Such sensors are located adjacent to rushing vehicles that result in a large amount of environmental noise. Passing vehicles and even wind can serve as a reliable source of acoustic energy that can be harvested for use by such sensors, thereby reducing the cost and physical size required to operate each sensor.

7.4.4 Microphones

One particularly impactful future application of this technology is microphones. Microphones are found in a wide variety of modern devices including audio recorders, smart home devices, and even more mechanical purposes such as internal combustion engine ”ping” or ”knock” sensors. All microphones are intended to capture a desired range of acoustic frequencies as part of their duties.

While microphones are quite effective at converting acoustic waves into electrical signals, they generally accomplish this task across their entire operational frequency range. This leads to a fairly even capture of all acoustic waves reaching the microphone, desirable and undesirable frequencies alike. However, all recording devices are limited in their dynamic range of loudest and quietest signals successfully captured. As such, the recorded signals can suffer from signal distortion or overload due to the presence of unwanted frequencies in the microphone’s environment.

Acoustic wave trapping can be used to design microphone structures that minimize the amplitude of undesirable frequencies while enhancing the amplitude of desirable frequencies. This is especially useful in microphone applications where a narrow range of captured frequencies is desired, such as internal combustion engine ping/knock sensors, since the acoustic wave trapping structure can be physically small. Such structures

could also provide substantial improvements to audio recording quality for broadcast microphones by isolating an instrument or subject's voice from unwanted noise that may be present in the recording environment such as road noise, HVAC handing equipment noise, or similar sounds with predictable frequencies.

The aforementioned applications merely represent a small subsection of the plethora of potential applications for acoustic rainbow trapping and energy harvesting technology. Additional applications currently exist for this technology, and others are in development.

References

[1] J. Brophy. (Feb. 2021). "Acoustic energy harvesting," [Online]. Available: https://www.acentech.com/blog/acoustic-energy-harvesting/.

[2] F. U. Khan and Izhar, "Electromagnetic energy harvester for harvesting acoustic energy," *Sadhana - Academy Proceedings in Engineering Sciences*, vol. 41, pp. 397–405, 4 Apr. 2016, ISSN: 09737677. DOI: 10.1007/s12046-016-0476-9.

[3] S. A. Cummer, J. Christensen, and A. Alù, "Controlling sound with acoustic metamaterials," *Nature Reviews Materials*, vol. 1, 16001 2016, ISSN: 20588437. DOI: 10.1038/natrevmats.2016.1.

[4] K. L. Tsakmakidis, A. D. Boardman, and O. Hess, "'Trapped rainbow' storage of light in metamaterials," *Nature*, vol. 450, pp. 397–401, 7168 2007, ISSN: 14764687. DOI: 10.1038/nature06285.

[5] J. Zhu, Y. Chen, X. Zhu, F. J. Garcia-Vidal, X. Yin, W. Zhang, and X. Zhang, "Acoustic rainbow trapping," *Scientific Reports*, vol. 3, 2013, ISSN: 20452322. DOI: 10.1038/srep01728.

[6] M. Yuan, Z. Cao, J. Luo, and X. Chou, "Recent developments of acoustic energy harvesting: A review," *Micromachines*, vol. 10, 1 Jan. 2019, ISSN: 2072666X. DOI: 10.3390/mi10010048.

[7] S. Qi, M. Oudich, Y. Li, and B. Assouar, "Acoustic energy harvesting based on a planar acoustic metamaterial," *Applied Physics Letters*, vol. 108, 26 Jun. 2016, ISSN: 00036951. DOI: 10.1063/1.4954987.

[8] N. Jiménez, V. Romero-García, V. Pagneux, and J. P. Groby, "Rainbow-trapping absorbers: Broadband, perfect and asymmetric sound absorption by subwavelength panels for transmission problems," *Scientific Reports*, vol. 7, 1 Dec. 2017, ISSN: 20452322. DOI: 10.1038/s41598-017-13706-4.

[9] J. M. De Ponti, "One-Dimensional Inhomogeneous Media," in *Graded Elastic Metamaterials for Energy Harvesting*, Cham: Springer, 2021, ch. 3, pp. 27–60, ISBN: 9783030690595. DOI: https://doi.org/10.1007/978-3-030-69060-1_3.

[10] B. Yang, H. Liu, and J. Liu, *Micro and Nano Energy Harvesting Technologies*. Artech House, 2014, ISBN: 9781608078158. [Online]. Available: http://ebookcentral.proquest.com/lib/rowan/detail.action?docID=1840893.

[11] D. G. Zhao, Y. Li, and X. F. Zhu, "Broadband lamb wave trapping in cellular metamaterial plates with multiple local resonances," *Scientific Reports*, vol. 5, 2015, ISSN: 20452322. DOI: 10.1038/srep09376.

[12] K. Donda, Y. Zhu, S. W. Fan, L. Cao, Y. Li, and B. Assouar, "Extreme low-frequency ultrathin acoustic absorbing metasurface," *Applied Physics Letters*, vol. 115, 17 Oct. 2019, ISSN: 00036951. DOI: 10.1063/1.5122704.

[13] H. Xinjing, Y. Yutian, M. Jinyu, L. Jian, and R. Xiaobo, "An acoustic metamaterial-based sensor capable of multiband filtering and amplification," *IEEE Sensors Journal*, vol. 20, pp. 4413–4419, 8 Apr. 2020, ISSN: 15581748. DOI: 10.1109/JSEN.2019.2962279.

[14] Z. Tian and L. Yu, "Rainbow trapping of ultrasonic guided waves in chirped phononic crystal plates," *Scientific Reports*, vol. 7, Jan. 2017, ISSN: 20452322. DOI: 10.1038/srep40004.

[15] N. Kazemi-Zanjani, M. Shayegannia, R. Prinja, A. O. Montazeri, A. Mohammadzadeh, K. Dixon, S. Zhu, P. R. Selvaganapathy, A. Zavodni, N. Matsuura, and N. P. Kherani, "Multiwavelength surface-enhanced raman spectroscopy using rainbow trapping in width-graded plasmonic gratings," *Advanced Optical Materials*, vol. 6, 4 Feb. 2018, ISSN: 21951071. DOI: 10.1002/adom.201701136.

[16] T. Chen, J. Jiao, and D. Yu, "Broadband acoustic enhancement and weak signals detection within a gradient acoustic-grating metamaterial," *Measurement: Journal of the International Measurement Confederation*, vol. 171, Feb. 2021, ISSN: 02632241. DOI: 10.1016/j.measurement.2020.108817.

[17] Z. Zhang, Q. Li, M. Oudich, Y. Pan, and Y. Li, "Experimental demonstration of enhanced acoustic energy harvesting with a subwavelength metamaterial plate," *New Journal of Physics*, Nov. 2020. DOI: 10.1088/1367-2630/abcce8.

[18] M. Yan, J. Lu, F. Li, W. Deng, X. Huang, J. Ma, and Z. Liu, "On-chip valley topological materials for elastic wave manipulation," *Nature Materials*, vol. 17, pp. 993–998, 11 Nov. 2018, ISSN: 14764660. DOI: 10.1038/s41563-018-0191-5.

[19] J. M. D. Ponti, A. Colombi, E. Riva, R. Ardito, F. Braghin, A. Corigliano, and R. V. Craster, "Experimental investigation of amplification, via a mechanical delay-line, in a rainbow-based metasurface for energy harvesting," May 2020, ISSN: 00036951. DOI: 10.1063/5.0023544. [Online]. Available: http://arxiv.org/abs/2005.04792.

[20] G. J. Chaplain, D. Pajer, J. M. D. Ponti, and R. V. Craster, "Delineating rainbow reflection and trapping with applications for energy harvesting," *New Journal of Physics*, vol. 22, 6 Jun. 2020, ISSN: 13672630. DOI: 10.1088/1367-2630/ab8cae.

[21] G. J. Chaplain, J. M. D. Ponti, G. Aguzzi, A. Colombi, and R. V. Craster, "Topological rainbow trapping for elastic energy harvesting in graded Su-Schrieffer-Heeger systems," *Physical Review Applied*, vol. 14, p. 054 035, 5 Nov. 2020, ISSN: 2331-7019. DOI: 10.1103/PhysRevApplied.14.054035. [Online]. Available: https://link.aps.org/doi/10.1103/PhysRevApplied.14.054035.

[22] J. M. D. Ponti, A. Colombi, R. Ardito, F. Braghin, A. Corigliano, and R. V. Craster, "Graded elastic metasurface for enhanced energy harvesting," *New Journal of Physics*, vol. 22, 1 2020, ISSN: 13672630. DOI: 10.1088/1367-2630/ab6062.

[23] H. Meng, D. Chronopoulos, N. Bailey, and L. Wang, "Investigation of 2D rainbow metamaterials for broadband vibration attenuation," *Materials*, vol. 13, pp. 1–9, 22 Nov. 2020, ISSN: 19961944. DOI: 10.3390/ma13225225.

[24] T. Liu, S. Liang, F. Chen, and J. Zhu, "Inherent losses induced absorptive acoustic rainbow trapping with a gradient metasurface," *Journal of Applied Physics*, vol. 123, 9 Mar. 2018, ISSN: 10897550. DOI: 10.1063/1.4997631.

[25] Z. Tian, C. Shen, J. Li, E. Reit, H. Bachman, J. E. S. Socolar, S. A. Cummer, and T. J. Huang, "Dispersion tuning and route reconfiguration of acoustic waves in valley topological phononic crystals," *Nature Communications*, vol. 11, p. 762, 1 Dec. 2020, ISSN: 2041-1723. DOI: 10.1038/s41467-020-14553-0. [Online]. Available: http://www.nature.com/articles/s41467-020-14553-0.

[26] M. Jin, B. Liang, J. Yang, J. Yang, and J. C. Cheng, "Ultrathin planar metasurface-based acoustic energy harvester with deep subwavelength thickness and mechanical rigidity," *Scientific reports*, vol. 9, p. 11 152, 1 Aug. 2019, ISSN: 20452322. DOI: 10.1038/s41598-019-47649-9.

[27] X. Ni, Y. Wu, Z. G. Chen, L. Y. Zheng, Y. L. Xu, P. Nayar, X. P. Liu, M. H. Lu, and Y. F. Chen, "Acoustic rainbow trapping by coiling up space," *Scientific Reports*, vol. 4, p. 7038, 2014, ISSN: 20452322. DOI: 10.1038/srep07038.

[28] M. Jasiewicz and K. Miadlicki, "An integrated cnc system for chatter suppression in turning," *Advances in Production Engineering & Management*, vol. 15, pp. 318–330, 3 Sep. 2020, ISSN: 18546250. DOI: 10.14743/apem2020.3.368.

[29] B. Ellis, *Chemistry and Technology of Epoxy Resins*, 1st ed. Dordrecht: Springer Netherlands, 1993, ISBN: 94-011-2932-0. DOI: 10.1007/978-94-011-2932-9.

[30] F. W. Isen, "DSP for MATLAB™ and LabVIEW™ I: Fundamentals of discrete signal processing," *Synthesis Lectures on Signal Processing*, vol. 3, pp. 1–213, 1 Jan. 2008, ISSN: 1932-1236. DOI: 10.2200/s000161ed1v01y200811spr004.

[31] K. Worden and J. M. Dulieu-Barton, "An overview of intelligent fault detection in systems and structures," *Structural Health Monitoring*, vol. 3, pp. 85–98, 1 2004, ISSN: 14759217. DOI: 10.1177/1475921704041866.

[32] M. R. Pearson, M. J. Eaton, R. Pullin, C. A. Featherston, and K. M. Holford, "Energy harvesting for aerospace structural health monitoring systems," vol. 382, Institute of Physics Publishing, 2012. DOI: 10.1088/1742-6596/382/1/012025.

[33] Y. Wang, X. Zhu, T. Zhang, S. Bano, H. Pan, L. Qi, Z. Zhang, and Y. Yuan, "A renewable low-frequency acoustic energy harvesting noise barrier for high-speed railways using a helmholtz resonator and a pvdf film," *Applied Energy*, vol. 230, pp. 52–61, Nov. 2018, ISSN: 03062619. DOI: 10.1016/j.apenergy.2018.08.080.

Appendix A

AEH Disc — Mechanical Specifications

Figure A1

AEH Disc — Waterjet Cutting Diagram

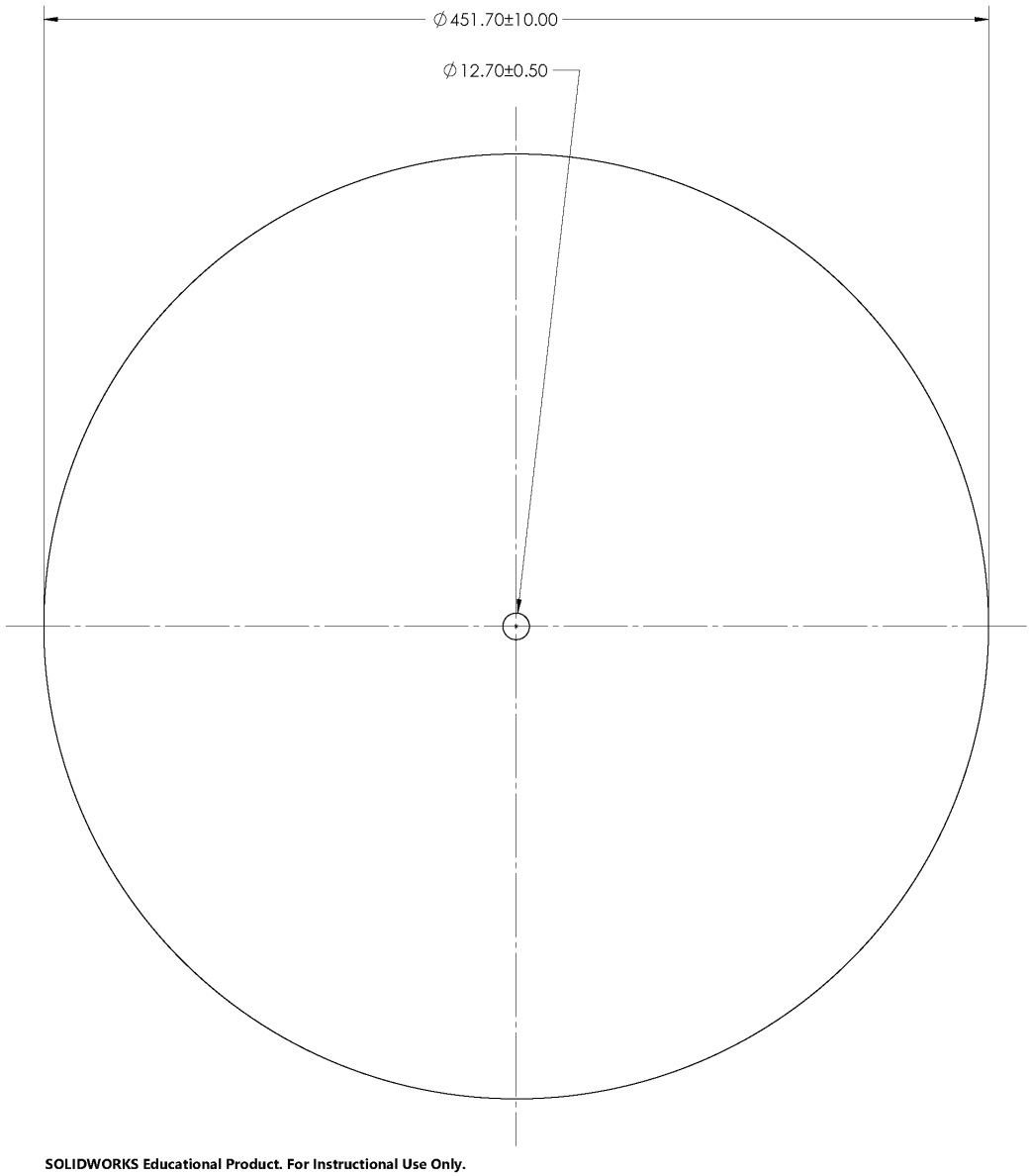

Figure A2

AEH Disc — Machining Drawing

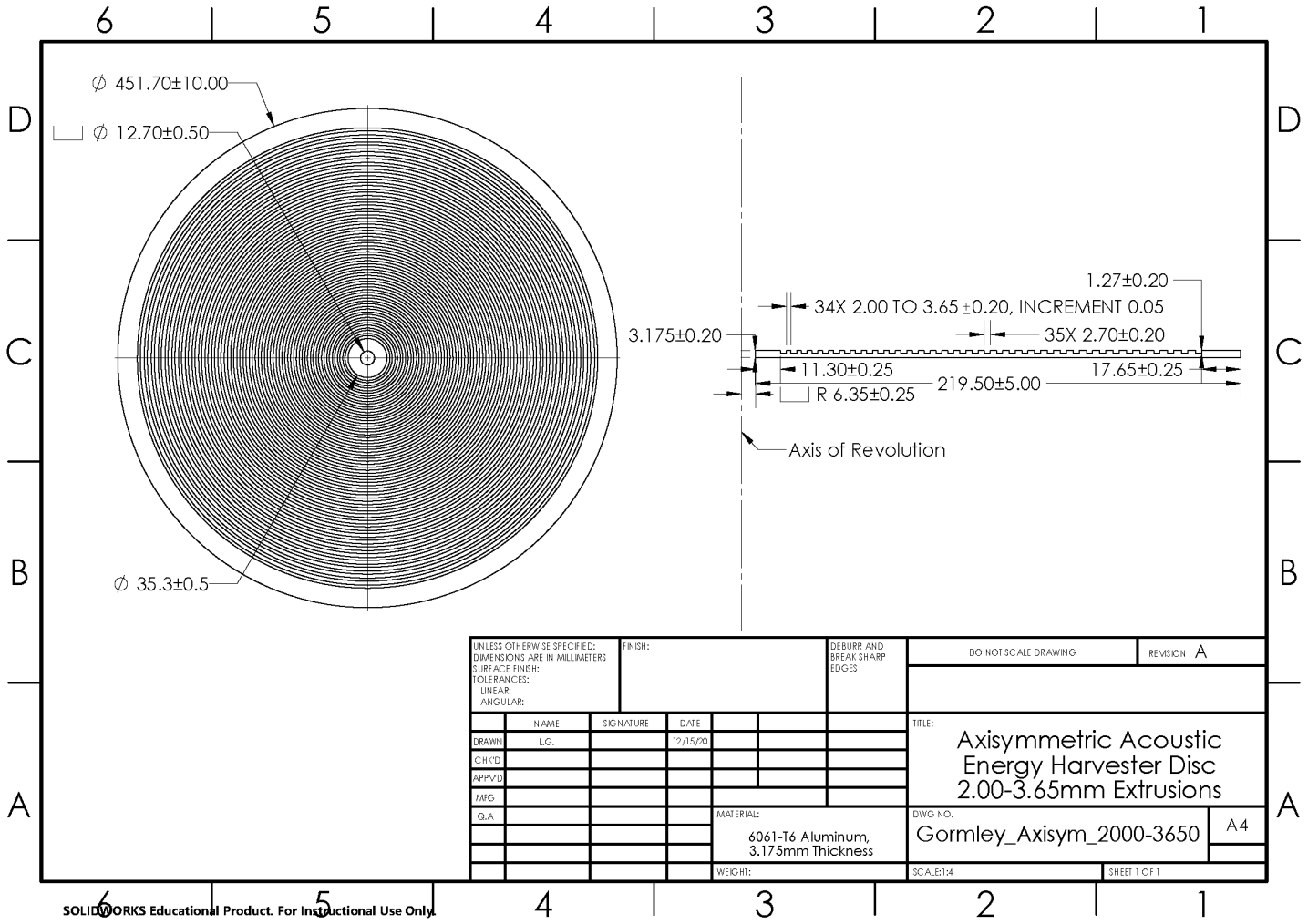

Appendix B

Induced Signal Generation MATLAB™ Code

```
1  function [gp, t]=sig_gaussian_pulse_int_14bit(freq, fs,
       tmax, tcenter, twidth)
2  % SIG_GAUSSIAN_PULSE(freq, fs, tmax, tcenter, twidth)
3  %   Creates a pulse having a gaussian envelope.
4  %   freq      Signal frequency components
5  %   fs        Sampling frequency
6  %   tmax      Signal length in seconds
7  %   tcenter   Center of the pulse
8  %   twidth    Width of the pulse for which the amplitude
       is
9  %             greater than 1% of the maximum value
10
11 t=1/fs:1/fs:tmax;
12 gp=sum(cos(2*pi*freq'*t),1).*exp(-4*log(10)/twidth^2*(t-
       tcenter).^2);
13 gp=round((gp+1)/2*(2^14-1));
```

Appendix C

Signal Command and Acquisition MATLAB™ Code

```
% Find a VISA-USB object - DG4162, function generator.
clear; clc;
dg4162 = instrfind('Type', 'visa-usb', 'RsrcName', 'USB0
    ::0x1AB1::0x0641::DG4E223101031::0::INSTR', 'Tag', '')
    ;

% Create the VISA-USB object if it does not exist
% otherwise use the object that was found.
if isempty(dg4162)
    dg4162 = visa('NI', 'USB0::0x1AB1::0x0641::
        DG4E223101031::0::INSTR');
else
    fclose(dg4162);
    dg4162 = dg4162(1);
end

dg4162.OutputBufferSize=512*1024; % Default is 512. For
    an arbitrary waveform, it will need larger buffer to
    transport the command
fopen(dg4162);

%% Find a VISA-USB object - DS1104, oscilloscope.
ds1104 = instrfind('Type', 'visa-usb', 'RsrcName', 'USB0
    ::0x1AB1::0x04CE::DS1ZD222100419::0::INSTR', 'Tag', ''
```

```
    );
% Create the VISA-USB object if it does not exist
% otherwise use the object that was found.
if isempty(ds1104)
    ds1104 = visa('NI', 'USB0::0x1AB1::0x04CE::
        DS1ZD222100419::0::INSTR');
else
        fclose(ds1104);
        ds1104 = ds1104(1);
end
% Connect to instrument object, ds1104.
ds1104.InputBufferSize=10000;
ds1104.OutputBufferSize=10000;

fopen(ds1104);

%% Initialize
ch_select = '1';    % check the connection on the
    waveform generator to confirm
voltage    = 25;    % voltage in Vpp
% This is a function to control the Waveform Generator,
    make sure the input
% is the (communication port, channel, frequency, and
    active time)

fprintf(dg4162, [':OUTP' ch_select ' ON']);

```

```
41 fs = 2.5e8; % DG 4162 has max output sampling rate of 500
     MHz, so fs<=5e8;
42 cyc_per_sigma = 10; % number of cycles within \sigma of
     Gaussian pulse
43 duty_cycle = 0.01; %value of duty cycle, must be within
     [0,1]
44
45 freq_init = 100e5; %start frequency, this is the main
     frequency (not the carrier wave frequency)
46 burst_period = 1/(freq_init/cyc_per_sigma*duty_cycle); %
     burst period
47 burst = [':BURS:INT:PER ' sprintf('%0.6f',burst_period)];
48 twidth = cyc_per_sigma/freq_init;
49 tmax = 2*twidth;
50 [sig,t_sig] = sig_gaussian_pulse_int_14bit(freq_init, fs,
      tmax, tmax/2, twidth);
51 % figure;plot(sig);
52 sig_String = sprintf('%.0f,' , sig);sig_String =
     sig_String(1:end-1); % convert the signal to a
     formatted string
53 fprintf(dg4162, [':SOUR' ch_select ':DATA:DAC volatile,',
     sig_String]);
54 fprintf(dg4162, [':SOUR' ch_select ':PERiod ' num2str(
     tmax)]); %% in s
55
56 % To set up the amplitude
57 fprintf(dg4162, [':SOUR' ch_select ':VOLT:UNIT VPP']); %
```

```
    % VRMS/VPP/DBM in Volts
58  fprintf(dg4162, [':SOUR' ch_select ':VOLT ' num2str(
    voltage)]); % setup input voltage
59
60  % use burst mode to generate a sequence of pulses
61  fprintf(dg4162, [':SOUR' ch_select ':BURS ON']); %turn on
     the burst mode
62  % fprintf(dg4162, [':SOUR' ch_select ':BURS:INT:PER
    0.0004']); %% set the burst period in s
63  fprintf(dg4162, [':SOUR' ch_select burst]); %% set the
    burst period in defined value
64  fprintf(dg4162, [':SOUR' ch_select ':BURS:TDEL 0']); %%
     Set the time from when the generator receives the
    trigger signal to starts to output the N cycle (or
    infinite) burst, in s
65  fprintf(dg4162, [':SOUR' ch_select ':BURS:NCYC 1']); %%
     Set the cycles of the burst.
66  fprintf(dg4162, [':SOUR' ch_select ':BURS:TRIG:TRIGO POS'
    ]); %% OFF|POS|NEG specify the edge type of the
    trigger output signal
67  %% generate signals
68  % The default input is sin wave with 5 Vpp amplitude. %
     change the
69  % parameters in the function to change o other source
    types.
70  % freqInput  = 150e3; % char in Hz, this is the main
    frequency (not the carrier wave frequency)
```

```
71 ch_select  = '1';    % check the connection on the
       waveform generator to confirm
72 voltage    = 25;     % voltage in Vpp
73 % This is a function to control the Waveform Generator,
       make sure the input
74 % is the (communication port, channel, frequency, and
       active time)
75
76 fprintf(dg4162, [':OUTP' ch_select ' ON']);
77
78 % To generate a sine wave (default)
79 % fprintf(dg4162, [':SOUR' ch_select ':FUNC SIN']);  %%
       Sine wave
80 % fprintf(dg4162, [':SOUR' ch_select ':FREQ ' num2str(
       freqInput)]);  %% in Hz
81
82 freq_start = 100e3; %start frequency, this is the main
       frequency (not the carrier wave frequency)
83 freq_increment = 2.0e3; %increment of frequency
84 freq_end = 220e3; %end frequency
85
86 for freqInput = freq_start:freq_increment:freq_end
87 num = (freqInput-freq_start)/freq_increment+1; %number of
       measurements
88 burst_period = 1/(freqInput/cyc_per_sigma*duty_cycle); %
       burst period
89 burst = [':BURS:INT:PER ' sprintf('%0.6f',burst_period)];
```

```
90 twidth = cyc_per_sigma/freqInput;
91 tmax = 2*twidth;
92 [sig,t_sig] = sig_gaussian_pulse_int_14bit(freqInput, fs,
       tmax, tmax/2, twidth);
93 % figure;plot(sig);
94 sig_String = sprintf('%.0f,' , sig);sig_String =
       sig_String(1:end-1); % convert the signal to a
       formatted string
95 fprintf(dg4162, [':SOUR' ch_select ':DATA:DAC volatile,',
       sig_String]);
96 fprintf(dg4162, [':SOUR' ch_select ':PERiod ' num2str(
       tmax)]); %% in s
97
98 % To set up the amplitude
99 fprintf(dg4162, [':SOUR' ch_select ':VOLT:UNIT VPP']); %
       % VRMS/VPP/DBM in Volts
100 fprintf(dg4162, [':SOUR' ch_select ':VOLT ' num2str(
       voltage)]); % setup input voltage
101
102 % use burst mode to generate a sequence of pulses
103 fprintf(dg4162, [':SOUR' ch_select ':BURS ON']); %turn on
       the burst mode
104 % fprintf(dg4162, [':SOUR' ch_select ':BURS:INT:PER
       0.001']); %% set the burst period in s
105 fprintf(dg4162, [':SOUR' ch_select burst]); %% set the
       burst period in defined value
106 fprintf(dg4162, [':SOUR' ch_select ':BURS:TDEL 0']); %%
```

```
    Set the time from when the generator receives the
    trigger signal to starts to output the N cycle (or
    infinite) burst, in s
107 fprintf(dg4162, [':SOUR' ch_select ':BURS:NCYC 1']); %%
    Set the cycles of the burst.
108 fprintf(dg4162, [':SOUR' ch_select ':BURS:TRIG:TRIGO POS'
    ]); %% OFF|POS|NEG specify the edge type of the
    trigger output signal
109
110 pause(5) %wait for 5 seconds for the signals to stablize
    and then read the signals
111
112
113     fprintf(ds1104, ':WAV:SOUR CHAN1');
114     fprintf(ds1104, ':wav:data?');
115     [data,len]= fread(ds1104,2048);
116     wave1(:,num) = data(12:len-1); %read signals of
          channel 1
117
118     fprintf(ds1104, ':WAV:SOUR CHAN2');
119     fprintf(ds1104, ':wav:data?');
120     [data,len]= fread(ds1104,2048);
121     wave2(:,num) = data(12:len-1); %read signals of
          channel 2
122
123     fprintf(ds1104, ':WAV:SOUR CHAN3');
124     fprintf(ds1104, ':wav:data?');
```

```
125         [data,len]= fread(ds1104,2048);
126         wave3(:,num) = data(12:len-1); %read signals of
                channel 3
127
128         fprintf(ds1104, ':WAV:SOUR CHAN4');
129         fprintf(ds1104, ':wav:data?');
130         [data,len]= fread(ds1104,2048);
131         wave4(:,num) = data(12:len-1);
132         time(num,:) = clock;
133         pause(1) %wait for another 3 seconds for the next
                measurement
134
135 end
```

Appendix D

Signal Processing MATLAB™ Code

```
1
2 %% Load signals, the measurement data for a complete run
      can be loaded so all the channels can be processed
3 close all
4 clear all
5 clc
6 load('run5.mat'); %load measurement
7 ch(1,:,:) = wave2;
8 ch(2,:,:) = wave3;
9 ch(3,:,:) = wave4;
10 ch(10,:,:) = wave1; %input signals are assigned to the
      last channel
11
12 load('run6.mat'); %load measurement
13 ch(4,:,:) = wave2;
14 ch(5,:,:) = wave3;
15 ch(6,:,:) = wave4;
16 ch(11,:,:) = wave1; %input signals are assigned to the
      last channel
17
18 load('run7.mat'); %load measurement
19 ch(7,:,:) = wave2;
20 ch(8,:,:) = wave3;
21 ch(9,:,:) = wave4;
```

```
22 ch(12,:,:) = wave1; %input signals are assigned to the
       last channel
23
24 [num,len,index] = size(ch); %check the size of the data,
      num is the number of sensors for a complete run, len
      is the number of signal points, index is the number of
       frequencies
25
26 radius = [3 5.1 7.2 9.3 11.4 13.5 15.6 17.7 19.8 1]; %
      distance from each sensor to the center, cm
27
28 for i = 1:num
29     for j = 1:index
30         ch(i,:,j) = ch(i,:,j)-mean(ch(i,:,j)); %clear the
               offset so that all the signals have a zero
              mean value
31     end
32 end
33
34 %% SAMPLING FREQUENCY ANALYSIS
35 freq = 100e3:2.0e3:220e3; %original is 100e3:2.5e3:250e3,
       the high frequency data is discarded
36 [freq_idx,freq_num] = size(freq);
37
38 sampling = zeros(num,index); %this is the sampling rate
      for each measurement
39 amp_idx = zeros(num,index); %this is the index point we
```

```
    should look at for the FFT amplitude
40  for i = 10:num
41      for j = 1:freq_num
42          for Fs = 4.0e6:0.01e6:8.0e6 %estimated sampling
                rate, check the original waveform to confirm
                it
43              Ts = 1/Fs;
44              Fn = Fs/2;
45              freqInput = freq(j); %this is the actual
                    frequency
46              fts = fft(ch(i,:,j))/len; %FFT
47              Fv = linspace(0, 1, fix(len/2)+1)*Fn;
48              Iv = 1:length(Fv);
49              amp_fts = abs(fts(Iv))*2; % Spectrum
                    Amplitude
50              [f_max,f_idx] = max(amp_fts); %find the
                    maximum, f_idx is the index, f_max is the
                    peak amplitude
51              if abs(Fv(f_idx)-freqInput)<=180
52                  if i==10
53                      sampling(i,j) = Fs;
54                      sampling(1,j) = Fs;
55                      sampling(2,j) = Fs;
56                      sampling(3,j) = Fs;
57                      amp_idx(i,j) = f_idx;
58                      amp_idx(1,j) = f_idx;
59                      amp_idx(2,j) = f_idx;
```

```
60                          amp_idx(3,j) = f_idx;
61                      elseif i==11
62                          sampling(i,j) = Fs;
63                          sampling(4,j) = Fs;
64                          sampling(5,j) = Fs;
65                          sampling(6,j) = Fs;
66                          amp_idx(i,j) = f_idx;
67                          amp_idx(4,j) = f_idx;
68                          amp_idx(5,j) = f_idx;
69                          amp_idx(6,j) = f_idx;
70                      elseif i==12
71                          sampling(i,j) = Fs;
72                          sampling(7,j) = Fs;
73                          sampling(8,j) = Fs;
74                          sampling(9,j) = Fs;
75                          amp_idx(i,j) = f_idx;
76                          amp_idx(7,j) = f_idx;
77                          amp_idx(8,j) = f_idx;
78                          amp_idx(9,j) = f_idx;
79                      end
80                  end
81              end
82          end
83  end
84
85  %% Analysis
86
```

```
87 for j = 1:freq_num
88     [up0,low0] = envelope(ch(num,:,j),30,'rms'); %find
          the envelopes of the input signals
89     [in_max(j),in_idx(j)] = max(up0);
90 end
91
92 for i = 1:num
93     for j = 1:1:freq_num
94
95         Fs = sampling(i,j);
96         Ts = 1/Fs;
97         Fn = Fs/2;
98
99         d_points = round(1*Fs./freq); %data points for
              one period for each frequency
100
101        num_cycle = 10; %nubmer of cycles to be included
              in the window, the input has 10 cycles
102        window = round(num_cycle/2*Fs./freq); %width of
              window to be applied to the signals
103
104        [up,low] = envelope(ch(i,:,j),30,'rms'); %find
              the envelopes of the signals
105        [pks,locs] = findpeaks(up); %find local peaks of
              the signals
106        a = size(locs);
107        if a(2) == 0 %no local maximum
```

```
108             if up(end)>up(1)
109                 locs = 1200;
110             end
111             if up(end)<up(1)
112                 locs = 1;
113             end
114         end
115         index0 = find(locs>in_idx(j),1,'first'); %find
                the first index that is greater than the input
                peak
116         b = size(index0);
117         if b(1) == 0
118             index0 = find(locs<in_idx(j),1,'last');
119         end
120         idx(i,j) = locs(index0); %index of the first peak
                after the peak index of the input signal
121         ch(i,1:idx(i,j)-window(j),j) = 0; %chop the
                signals so that they only contain information
                within the window
122         ch(i,idx(i,j)+window(j):end,j) = 0;
123         fts = fft(ch(i,:,j))/len; %FFT
124         Fv = linspace(0, 1, fix(len/2)+1)*Fn;
125         Iv = 1:length(Fv);
126         amp_fts = abs(fts(Iv))*2; % Spectrum Amplitude
127         amp_fts_meas(j,:,i) = amp_fts;
128         phs_fts = angle(fts(Iv)); % Spectrum Phase
129         amp(i,j) = amp_fts(amp_idx(i,j));
```

```
130             phase(i,j) = phs_fts(amp_idx(i,j));
131         end
132 end
133
134 %% AMPLITUDE NORMALIZATION PROCESSING
135 freq_interest=transpose(1:10:61); %FREQUENCIES OF
        INTEREST: 100-220 KHZ, EVERY 20 KHZ
136 amp_fts_meas01=amp_fts_meas(freq_interest,:,1); %AMP_FTS
        @ FREQ. OF INTEREST: SENSOR 01
137 amp_fts_meas10=amp_fts_meas(freq_interest,:,10); %AMP_FTS
         @ FREQ. OF INTEREST: SENSOR 10
138 amp_fts_norm0110=amp_fts_meas01./amp_fts_meas10; %
        NORMALIZE AMPLITUDE OF SENSOR 01 VS SENSOR 10 INPUT
139 freq_interest=freq_interest*2e3+98e3;
140
141 %% NORMALIZED AMPLITUDE VS FREQ PLOT
142 figure
143 plot(Fv,amp_fts_norm0110(:,:))
144 xlabel('Frequency (kHz)','FontSize',12,'FontWeight','bold
        ');
145 ylabel('Amplitude (V)','FontSize',12,'FontWeight','bold')
        ;
146 xlim([180e3 240e3]);
147 xticks(100e3:50e3:250e3);
148 xticklabels({'100','150','200','250'});
149
150 %% Plot data
```

```
figure
for i = 1:5
    plot(freq,amp(i,:)*35,'LineWidth',2); % Oscilloscope
        scale: 35mV
    hold on
end
xlabel('Frequency (kHz)','FontSize',12,'FontWeight','bold
    ');
ylabel('Amplitude (mV)','FontSize',12,'FontWeight','bold'
    );
xlim([100e3 220e3]);
xticks([100e3 150e3 200e3 250e3]);
xticklabels({'100','150','200','250'});
legend('Sensor1','Sensor2','Sensor3','Sensor4','Sensor5')
    ;

figure
for i = 6:9
    plot(freq,amp(i,:)*35,'LineWidth',2); % Oscilloscope
        scale: 35mV
    hold on
end
xlabel('Frequency (kHz)','FontSize',12,'FontWeight','bold
    ');
ylabel('Amplitude (mV)','FontSize',12,'FontWeight','bold'
    );
xlim([100e3 220e3]);
```

```
171 xticks([100e3 150e3 200e3 250e3]);
172 xticklabels({'100','150','200','250'});
173 legend('Sensor6','Sensor7','Sensor8','Sensor9');
```